Autonomous Temperature Sensor for Smart Agriculture

Energy Harvesting and Control

M.D. Hubers

R.P.J. van der Sande

TU Delft Delft University of Technology

June 2020

Autonomous Temperature Sensor for Smart Agriculture

Energy Harvesting and Control

by

M.D. Hubers, 4608925

R.P.J. van der Sande, 4690311

Delft University of Technology

Faculty of Electrical Engineering,
Mathematics and Computer Science

In partial fulfilment of the requirements for the degree of

Bachelor of Science
In Electrical Engineering

To be defended in public on 30 June 2020 at 9:00 AM

Supervisors:	Dr. Q. Fan	
	Ing. R.M.A. van Puffelen	
	MSc. L. Pakula	
Thesis committee:	Prof.dr.ir. P. Bauer	TU Delft
	Ing. R.M.A. van Puffelen	TU Delft
	Dr. Q. Fan	TU Delft
	Dr. M. Ghaffarian Niasar	TU delft
	MSc. L. Pakula	TU Delft

Abstract

Many countries in the world face the problem of fruit frost during spring, which results in the loss of harvested crops. Solutions exist to prevent the fruit to freeze, however this requires that the temperature is known. Therefore, a smart autonomous temperature sensor network is designed that is capable of acquiring a 3D temperature profile of a fruit orchard to detect fruit frost. This thesis discusses the design of the energy harvesting and control module, which is one of the three sub-modules of the system. The goal is to sustain the energy demands of the sensor in a durable way, in order to operate for 20 years without requiring maintenance. To achieve this, several ambient energy sources and their harvesting techniques are investigated and simulated to examine the energy that can be harvested. This resulted in the use of solar energy, harvested by a solar cell and controlled by a maximum power point tracking module. Next, different energy storage implementations are considered to store the harvested energy temporarily. The use of a 5 F supercapacitor is concluded. Furthermore, an energy monitoring circuit is designed to measure the energy stored in the supercapacitor. Full system reliability simulations are done to verify the complete design by utilising the solar irradiance and temperature data of the past ten years. From these simulations is concluded that the design can sustain the energy demands of the sensor at all times.

Preface

For the past three months, we have been fully committed to the "Autonomous Temperature Sensor for Smart Agriculture' project. Lying in front of you is the result, the thesis 'Energy Harvesting and Control', in which we describe our design steps that we have taken to get to the final implementation. As the Energy Harvesting and Control group, we are responsible for the sustainable harvesting and storage of ambient energy, that is part of an exciting and rapidly developing field of engineering which is of great social interest.

This thesis is written as part of our graduation project, for the degree of Bachelor of Science in Electrical Engineering at Delft University of Technology. The research done in this project has been conducted as part of the Electronic Instrumentation group.

Our process started with the theoretical research on ambient energy sources, their harvesters and possible implementations. After this, we continued with the simulation of our findings. But because this project took place in the time of the coronavirus, even-though normally required, no physical demonstrator is build or physical measurements are conducted. Although this was not the optimal starting point, we think that we have managed to come up with a great and very well justified design in which the design choices are substantiated with elaborate computer simulations.

We first of all would like to extend our gratitude to our supervisors, Dr. Q. Fan, Ing. R.M.A. van Puffelen, and MSc. L. Pakula. They provided us with excellent guidance and constructive advice throughout the project. We truly enjoyed working together and learned a lot from their expertise. Also, we would like to thank Dr.ing. I.E. Lager for his excellent organisation of the bachelor graduation project, especially considering the quick adaption to the current circumstances.

Further, we want to thank our project group members and friends, Arnoud Bleeker, Michael Miao, Martijn Huiskes and Ruben Wijnands. We have found it a pleasure to be part of this team with great skill, clear communication and endless motivation.

We hope you enjoy reading this thesis.

Martijn Hubers and Robin van der Sande

Delft, June 2020

Contents

List of abbreviations

ADC	Analog to digital converter
DC	Direct current
DOD	Depth of discharge
EDLC	Electric double layer capacitors
EOC	End of charge
ESR	Equivalent series resistance
IO	Input/output
IOT	Internet of things
LDO	Low dropout regulator
Li-ion	Lithium-ion
MCU	Microcontroller unit
MOSFET	Metal oxide semiconductor field effect transistor
MPP	Maximum power point
MPPT	Maximum power point tracking
NiCad	Nickel-cadmium
NiMH	Nickel-metal-hydride
PV	Photovoltaic
RF	Radio frequency
ROI	Return on investment
STC	Standard test conditions
TEG	Thermoelectric generator
UVP	Under voltage protection
Wp	Watt peak

Chapter 1

Introduction

In the Netherlands fruit production is a large segment of the economy. There are over 2600 fruit production companies which together use over 20,000 hectares of ground [1]. Most of these Dutch companies focus on the production of pears and apples. The fruit production in the Netherlands, but effectively all around the world, faces a large problem related to spring frosts in fruit trees. If temperatures drop below the critical temperature, flower buds, as well as open and blooming flowers of the fruit trees, can be damaged causing less fruit to grow. The frost damages are mainly caused by the formation of ice. Intra-cellular ice formation breaks the blossom's tissue structure and causes a cell death [2]. Freeze injury is nowadays the biggest problem of fruit production, which causes a loss far greater than any other type of natural hazard encountered with the production. As a result, the yield of production and distribution of fruits are reduced.

A lot of research has been done in order to obtain a reduction in the losses caused by spring frosts. Two of the main solutions that are provided are frost protection with sprinkler irrigation and frost protection with wind machines. The frost protection with sprinkler irrigation works using extra-cellular ice formation to prevent intra-cellular ice formation. Sprinkling water onto the tree's flowers and buds cause ice nucleation on the outer surface. This causes the freezing of the water transporting vessels which protects the flowers due to gradual dehydration [3]. Frost protection with wind machines aims at the prevention of intra-cellular ice formation. By using a large wind machine or rotating fan a light wind (1.5 m/s) is created which causes an instantaneous increase in temperature [4]. Because of the fan, a temperature increase is obtained of up to 1 °C at a 15 m distance from the wind machine. Due to this small increase, the flowers are protected from the frost.

1.1 The project

So now there are two effective solutions used to prevent spring frosts in fruit trees. Both of these solutions have a requirement to know the temperature of the air surrounding the trees, and their control systems make decisions based on these temperature measurements. But in order to implement these solutions in large scale fruit production companies, an accurate temperature measurement is required over the whole field, rather than one single temperature measurement. Therefore this project focuses on the acquisition of the 3D temperature profile of a fruit orchard in the temperature range near the critical temperature of the fruit.

The great advantage of the acquisition of the temperature profile in contrast to a single temperature measurement is that it provides the ability to perform local frost protection rather than frost protection over the whole field. This in turn provides a reduction of the use of resources such as water and electric energy. In addition, the acquisition of the temperature profile provides a valuable resource for further research on the effectiveness of the frost protection methods.

In Figure 1.1 an overview of the wireless sensor network is shown. This sensor network consists of multiple sensor nodes. A sensor node consists of an energy harvesting module, an MCU, a wireless communication module, and five temperature sensors, which are all integrated onto a pole as shown in Figure 1.1a. The poles are positioned among the trees of the fruit orchard, and together they form a smart wireless temperature sensor network in the fruit orchard, as shown in Figure 1.1b. In Appendix A.1 the choice of this implementation is explained.

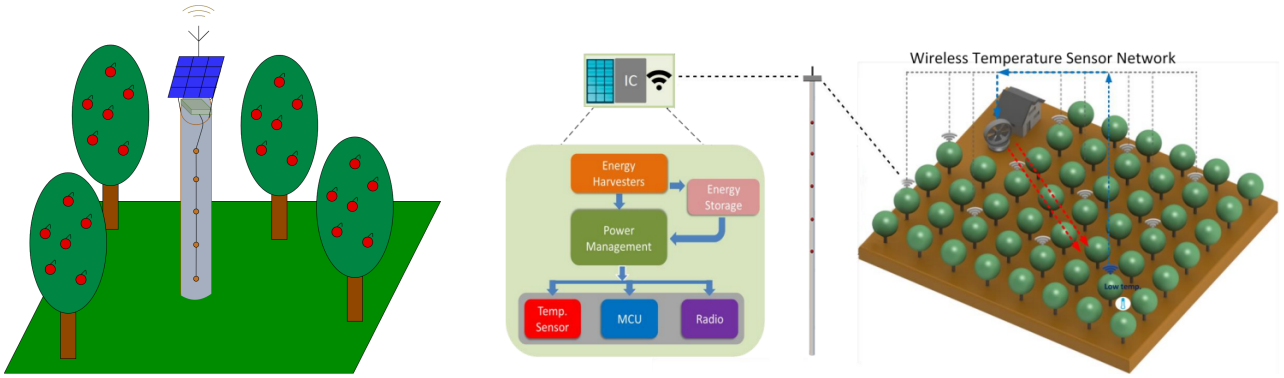

(a) The implementation of the sensor node on a pole placed in between trees of a fruit orchard. *(b) Zooming out from the individual modules of the sensor node to the wireless sensor network as a whole.*

Figure 1.1: Overview of the pole and system implementation.

1.2 Energy harvesting and control

The "Autonomous Temperature Sensor for Smart Agriculture" project is divided into three subgroups, each focusing on different tasks to realise the design of the wireless sensor network. The Smart Measurement and Control group is responsible for measuring the temperature, processing this data for wireless transmission and adapting the measurement frequency in a smart manner to form a smart network, see [5] for their thesis. The Wireless Communication group is responsible for a network design such that reliable data transmission takes place between the sensor nodes and the end user, see [6] for their thesis. The Energy Harvesting and Control group is responsible for the harvesting of energy from an ambient energy source, storing this energy locally in a storage module, distribute power to the modules of the other two subgroups, and measuring the energy level of the energy storage. In Figure 1.2 a schematic overview of the connections between the different subgroups is shown, together with the individual modules of the Energy Harvesting and Control group.

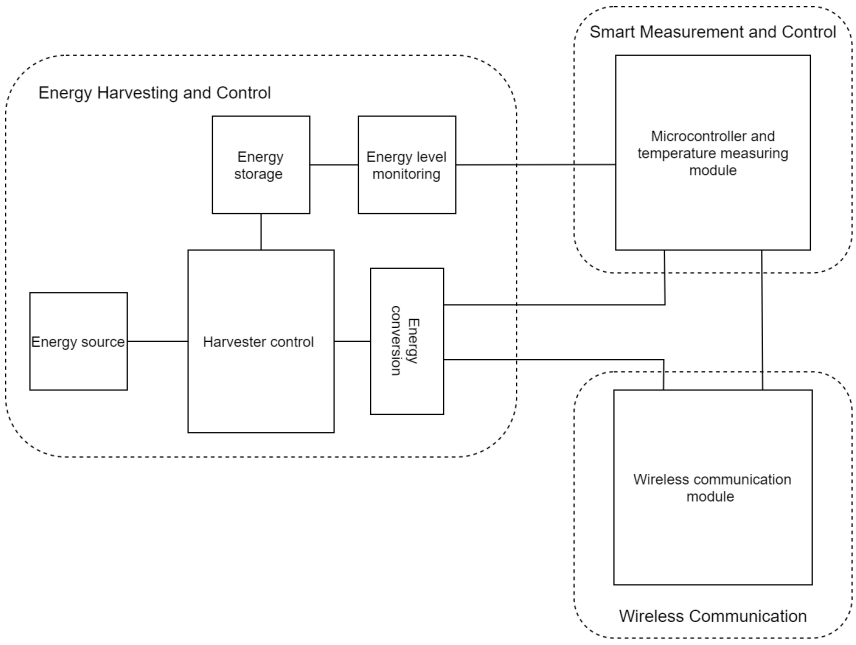

Figure 1.2: Overview of the connection between the different subgroups and the modules of energy harvesting and control group.

1.3 State of the Art

So to prevent fruit crop losses due to frost, the goal is to design a smart wireless temperature sensor network that is able to warn the farmer when parts of the fruit orchard reach a threshold temperature. Such a network can be classified as an Internet of Things network (IoT). An IoT device consists of four main building blocks, which are the main control units, sensors, communication modules and power sources [7]. Since this project requires a solution which makes use of these four main components and is used in agriculture, the device which is designed can be classified under IoT for smart agriculture.

Currently, the use of labour is often needed to measure and monitor the temperature on a farm, and frost protection equipment is activated manually when a critical temperature is measured [8]. Research conducted by Ghaemi et al. [3] shows a successful implementation of automated irrigation systems for protecting blossom on peach and orange trees, where a few thermistors were connected by wires on a height of 1.5 m above ground level to measure temperature. Pierce et al. [8] implemented an on-farm wireless sensor network, which provides real-time monitoring of the temperature with an accuracy of 0.1 $°C$ where an alarm is triggered if the temperature reaches a predetermined threshold, and is powered by a battery and optionally by a solar panel. In the work of Sushanth et al. [9], an IoT solution is proposed which consists of a solar powered Arduino board, where its temperature, humidity, and soil moisture sensors are connected by wire to this Arduino. If action is required, a message is sent to an Android application.

In the above described solutions of Ghaemi et al. [3] and Sushanth et al. [9], the sensors are connected by wire to some form of a base station. When many sensors are distributed over a large orchard, in case of a 3D temperature profile, this will result in a lot of wiring. Also, possible maintenance costs will increase when wires get disconnected. Therefore, a wireless sensor network solution is proposed. Furthermore, a solution is proposed which focuses on energy harvesting instead of battery operated only, since battery-operated solutions go together with maintenance costs, for example periodic replacement of batteries, and have a limited lifetime. Furthermore, the individual nodes of the above proposed solutions are not able to work together in a smart manner to form a smart system. These requirements finally lead to the design of a wireless, self-sustainable smart sensor network.

1.4 Structure of the thesis

First, the program of requirements is given in Chapter 2. Next, the energy source module is specified in Chapters 3 and 4, where the choice of the ambient energy source and of the corresponding harvesting device is explained, respectively. Chapter 4 also deals with the harvester control module, which is used to optimally harvest energy from the source. Further, this chapter specifies the energy conversion module, which is used to supply power to the other subgroups. In Chapter 5 the energy storage module is elaborated, in which a choice of the type and size of energy storage is made. In this chapter the design of the energy level monitoring module is elaborated as well. The implementation and integration of the harvester control module with the other modules is given in Chapter 6. Also, a reliability analysis of the power availability of a complete sensor node is made in this chapter, based on weather data of the past ten years. Finally, conclusions and future work for improvement are given in Chapter 7.

Chapter 2

Program of requirements

In order to achieve the goal of acquiring a 3D temperature profile of a fruit orchard, the whole sensor network and the individual sensor modules must comply with certain requirements. These requirements are classified as functional and nonfunctional requirements. A functional requirement describes a certain function the sensor network or an individual sensor module must perform in order to achieve the required goal. These requirements are listed below.

	General functional requirements	**Justification**
G1.	The sensor network must operate remotely in the fruit orchard	Primary project function
G2.	The sensor network must generate a 3D temperature map	Primary project function
G3.	The sensor module must measure the temperature	Primary project function
G4.	The rate of temperature measurements must be able to vary	Rate of temperature measurements depends on the change of temperature
G5.	The measured data must be stored	Primary project function
G6.	The sensor module must contain an energy harvesting unit, that is capable of sustaining all power requirements of the system.	Primary project function
G7.	The sensor module must contain an energy storage unit, that is capable of sustaining the continuity of the power delivery.	Required to guarantee continuity of operation
G8.	The sensor network must be scalable in terms of the amount of nodes it can support	The sensor network has to be deployed in different sizes of farms
G9.	The sensor module must be scalable in terms of the amount of functions it can perform	For the usability of the sensor nodes
G10.	The sensor module must be able to do data processing in a smart manner	Primary project function
G11.	The sensor module must be operational after a period of no incoming energy	Primary project function
G12.	The energy level of the energy storage should be monitored	Required for adaptive management
G13.	The sensor network must be able to warn the farmer when frost prevention action is required	Primary project function

The non functional requirements quantify the sensor modules, define how the sensor network and the sensor modules should be deployed, and describe which specifications they should have in order to acquire a 3D temperature map. These are listed below.

	General nonfunctional requirements	Justification
G14.	The density of sensors must be one sensor module per 100 m^2	Primary project function
G15.	One sensor module must consist of five temperature sensors	Required to obtain an accurate 3D temperature map
G16.	The temperature sensors must be evenly distributed over the height range	Required to obtain an accurate 3D temperature map
G17.	The temperature sensors of each sensor module should be placed at the same height with respect to the temperature sensors of the other sensor modules	Required to obtain an accurate 3D temperature map
G18.	The minimal temperature range of operation is -10 °C to 10 °C	Primary project function
G19.	The temperature measurement accuracy is 0.5 °C in the temperature range of operation	Primary project function
G20.	The system should have a lifespan of at least 20 years in normal operation conditions.	In order for the investment to have a positive ROI
G21.	The system is designed to be used in Europe for an average fruit orchard of 10 ha	Primary project function
G22.	The cost price per sensor node must be in the range of €100,-	In order for the investment to have a positive ROI
G23.	The system is designed to operate during spring	During this time flower buds are present as well as night frost

In addition to the requirements which must be complied with by the whole sensor network and the individual sensor modules, there are requirements specifically for the energy harvesting and control module. These requirements define the anticipated interactions with the wireless communication unit and the microprocessor. Also, requirements are set on the sustainability of the solution. These requirements are listed below.

	Energy harvesting, storage and control requirements	Justification
E1.	The module must provide an output voltage of 1.8 V to the microcontroller	Requirement from the microcontroller group[1]
E2.	The module must provide an output voltage of 3.3 V to the wireless communication unit	Requirement from the wireless communication group[1]
E3.	The module must provide instantaneous peak power of 14.25 mW to the microcontroller	Requirement from the microcontroller group[1]
E4.	The module must provide instantaneous peak power of 120.45 mW to the wireless communication unit	Requirement from the wireless communication group[1]
E5.	The module must provide average power of 3.31 μW to the microcontroller	Requirement from the microcontroller group[1]
E6.	The module must provide average power of 5.28 μW to the wireless communication unit	Requirement from the wireless communication group[1]
E7.	The energy required for one extra transmission is 13.8 μWh	Requirement from the wireless communication group[1]
E8.	The energy harvesting must be sustainable	Primary project function
E9.	The energy storage must be sustainable	Primary project function
E10.	The energy storage should be capable of storing sufficient energy for the sensor node to operate for two days without any incoming energy	The sensor module must be used after a period of no incoming energy as stated by G11

[1]The values mentioned in these specification are determined by a consultation and consideration between the energy harvesting and control group, microcontroller group and wireless communication group [5] [6]. More details can be found in Appendix A.3.

Chapter 3

Ambient energy source

The autonomous temperature sensor network can consist of thousands of individual sensor nodes, as mentioned in Section 1.1. These nodes all consist of a processor, a communication module and five temperature sensors which need energy to perform their operation. In contrast to obtaining this energy from a battery, for this project each sensor node must be able to locally harvest its required energy. This choice reduces the replacement cost of energy storage, increases continuity of operation, and on top of that makes the sensor node more environmentally friendly.

For the local energy harvesting at the sensor nodes, there are multiple types of ambient energy sources that can be used. The first one being solar energy. This type of energy involves the energy transmission from the sun by using electromagnetic radiation and can be harvested by exploiting the photo-voltaic effect in solar cells. Second, Radio Frequency (RF) energy, this type of energy is present in the form of radio waves that propagate through space. These waves are signified by time-varying electric and magnetic fields that are oscillating in the frequency range from around 20 kHz to 300 GHz. The waves are created as the result of ambient sources such as wireless telecommunications like WiFi and Bluetooth. Third, wind energy can be used as an ambient energy source for the sensor nodes. Wind energy can be seen as a secondary solar energy source and can be harvested in various ways such as with turbines, piezoelectric materials or aeroelastic flutter generators (a.f.g.). Finally, electric energy can be obtained from thermal energy. The conversion is done using thermoelectric generators that exploit the Seebeck effect.

In this chapter, the focus is put on the choice of which ambient energy source is used to power the sensor nodes. In Appendix B a more detailed description is given of the different types of ambient energy sources, their properties and the way they are harvested.

3.1 Comparison of energy sources

The ambient sources with their properties and harvesting techniques are summarised in Table 3.1. This section focuses on the comparison of these ambient energy sources and their harvesters concerning their degree of compliance with requirements G1, G6, G20 and E8. To come to a structured design conclusion, the six energy harvesting methods are compared to and weighed against each other based on different criteria.

Table 3.1: Overview of the properties of ambient energy sources [10] [11] [12] [13].

Source	Harvesting technique	Power density	Availability	Efficiency
Solar	Solar cell	100 mW/cm^2	Daytime and weather dependent	5%-30%
RF	RF harvester	1 $\mu W/cm^2$	All day	30%
Wind	Turbine/ a.f.g.	1 mW/cm^2	Weather dependent	35%
	piezoelectric	200 $\mu W/cm^3$	Weather dependent	20%
Thermal	Thermoelectric generator	60 $\mu W/cm^2$	Weather dependent	1-15%

Power density

The power density is defined as the available power per unit area or per unit volume provided by the source. This is regarded as the most important criterion, since it determines the maximum peak power that can be harvested. The power density needs a certain threshold value in order to harvest enough energy for the sensor node to operate, thus complying with requirement G6. With the aid of Table 3.1 it can be concluded that solar energy has the highest power density thus scores the highest. The power density is 100 mW/cm^2

in case of direct illumination and optimal weather conditions. RF energy has the lowest power density thus scores the lowest.

Continuality

The continuality is defined as the distribution of the power delivery of the source over a time span of one day. This is regarded as the least important criterion, since a storage unit is used to compensate for discontinuities during the day. It is assumed here that the source has enough power density and availability to harvest enough energy to meet the daily energy consumption of the sensor node. RF energy scores the highest, since the sources of RF energy transmit continuously and can therefore always be harvested. Thermal energy scores the lowest, as most of the time there will not be a large enough temperature differences present to harvest energy [11]. Further, solar energy can only be harvested during the day, and the energy that can be harvested is strongly affected by the presence of clouds. Therefore, solar energy scores low. The three wind energy harvesters score the same since they all depend equally on the wind and its continuality.

Availability

The availability is the total time in one day the source can be harvested. This is regarded as the second most important criterion, as the energy source should be available for a sufficient time to harvest enough energy for the sensor node to operate. For the same reasoning as with the continuality, RF energy scores the highest while thermal energy scores the lowest. For solar energy, on average there are only 2.7 solar hours available a day in the Netherlands [14]. The three wind energy harvesters score again the same since they all depend equally on the wind and its availability.

Price

The price of the energy harvester should be considered to satisfy requirement G22, and to reduce the overall cost of the system implementation. However, the focus is set on satisfying requirement G6 and not reducing the cost of the system, thus is not very important. Solar energy scores the highest, as solar cells cost between €0.56 and €1.07 per Watt-peak (Wp)[1], thus are relatively cheap [15]. RF energy and piezoelectric harvesting both score the lowest, as RF energy requires complicated and expensive hardware, and piezoelectric material is expensive.

Implementation difficulty

The implementation difficulty is defined as the time to produce and install the energy harvester, and the number of components needed. However, as this is only a first iteration, the focus should not revolve around this metric. Solar energy and RF energy both score the highest. Solar cells need to be placed with the correct orientation to the sun and need a maximum power point tracking (MPPT) module, while an RF harvester consists only of an antenna which is connected to an RF harvesting module and can be placed with any orientation. Piezoelectric energy scores the lowest, as this needs to be mounted onto moving parts, for example the branches of a tree, to harvest energy. The aeroelastic flutter generator also scores low. This harvester is placed stationary, but since it needs an orthogonal orientation to the wind direction, harvesting energy for different wind directions becomes difficult. Moreover, it is not readily available on the market. A wind turbine also needs an orthogonal orientation to the wind, but is readily available on the market and scores therefore 1 point higher. Thermal energy scores high, as it consists only of two plates of thermoelectric material and a thermoelectric module thus is easy to install, and is readily available.

Reliability

The reliability is defined as the robustness of the harvester. This is regarded the third most important criterion, as the system has to operate for at least 20 years as specified by requirement G20. Thermal, RF, and solar energy score the highest, as they all consist of stationary parts only. Due to the simplicity of a thermoelectric generator, it only degrades due to ageing [16]. Further, solar cells manufactures provide often 25-year warranty, and Jordan et al. [17] has shown that over a period of 20 years only 1.30% of 2083 solar panels failed. The three methods to harvest wind energy score very low. This is due to the fact

[1]Watt peak is a measure of the performance of a solar panel: the converted power if the panel is exposed to STC[2]
[2]Standard test conditions (STC) means 1000 W/m^2 of incoming radiation at 25 °C with an air mass 1.5

that they all consist of moving parts, which wear down over time. Echavarria et al. [18] has shown that large wind turbines, in the MW range, fail two to three times a year due to component breakdown. Further, piezoelectric material is brittle and susceptible to accidental breakage [19].

Efficiency of harvesting

The efficiency of the energy harvester is also of importance as this specifies how effective the incident power density can be converted. The efficiency thus affects the amount of energy that can be harvested. From Table 3.1 can be concluded that a wind turbine and an aeroelastic flutter generator have the highest efficiency, thus both score the highest, while thermal energy scores the lowest.

Final decision

A comparison table is made based on the previous discussion in order to select the energy source that is most suitable, and is shown in Table 3.2. Each criterion is assigned a weight from 1 to 10 based on its importance, where 10 is the most important. The different energy sources and harvesting techniques are then given a score from 1 to 10 for each criterion, where 10 is the best. The highest weighted sum of the scores then gives an indication of the most suitable option.

Table 3.2: Comparison table of different ambient energy sources and harvesting techniques that can be used for energy harvesting.

		Solar Energy		**RF Energy**		**Wind turbine**	
Criterion	**Weight**	**Score**	**Weighted**	**Score**	**Weighted**	**Score**	**Weighted**
Power density	9	10	90	1	9	5	45
Continuality	2	2	4	10	20	5	10
Availability	8	6	48	10	80	7	56
Price	3	8	24	2	6	4	12
Implementation difficulty	3	9	27	9	27	4	12
Reliability	7	9	63	9	63	3	21
Efficiency of harvesting	5	6	30	7	35	8	40
			286		240		196

		Piezoelectric energy		**Aeroelastic f.g.**		**Thermal energy**	
Criterion	**Weight**	**Score**	**Weighted**	**Score**	**Weighted**	**Score**	**Weighted**
Power density	9	3	27	5	45	2	18
Continuality	2	5	10	5	10	1	2
Availability	8	7	56	7	56	1	8
Price	3	2	6	3	9	6	18
Implementation difficulty	3	2	6	3	9	8	24
Reliability	7	2	14	3	21	9	63
Efficiency of harvesting	5	5	25	8	40	4	20
			144		190		153

As can be concluded from the table, solar energy results in the best option as it has the highest weighted score of 286. However, RF energy also scores relatively high compared to the other sources and is also a good option, mainly because of its high continuality and availability. Furthermore, a wind turbine also has potential as it scores average on almost all criteria. A wind turbine has the advantage over the aeroelastic flutter generator and piezoelectric harvester that it is more reliable and more widely available, which also gives the better price. Since the tree wind harvesters have approximately the same incident energy density and availability, the turbine is seen as the best wind energy harvester for this application. Therefore solar energy, a wind turbine and RF energy are considered, and further analysis is done to make a choice.

3.2 Performance and selection of the energy source

In the previous section is concluded that thermal energy and wind energy harvested using aeroelastic flutter or piezoelectric generators are no viable solutions. In this section, a more detailed performance analysis is given on the application of a wind turbine as harvesting technique, as well as RF energy or solar energy as the ambient energy source of the sensor nodes.

3.2.1 Performance evaluation wind turbine

The performance of a small wind turbine is evaluated by first making an estimate of the energy that can be harvested to see if it can comply with requirement G6. This estimate of the average power that can be harvested per month by a small wind turbine is made using Equation 3.1, for which the derivation is given in Appendix B. The average wind speed per month in the province Flevoland between the years 1981-2010 is used as the wind speed v [20]. Also, a propeller radius of 7 cm is used, which is reasonable considering the fact that the system is mounted onto a pole. Finally, the theoretical maximum of 0.59 is used for C_p. In Figure 3.1 the average power estimation for each month is shown.

$$P_{tur} = \frac{1}{2} C_p A \rho v^3 \tag{3.1}$$

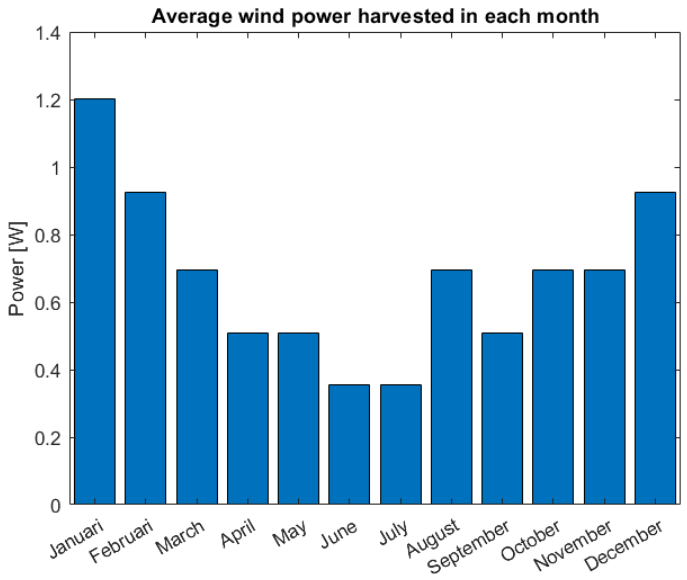

Figure 3.1: Estimation of the average power that can be harvested per month in the province Flevoland using a wind turbine with a propeller radius of 7 cm.

From Figure 3.1 and Appendix A.3 can be concluded that a reasonable amount of power can be harvested during each month such that the sensor nodes can perform their operations. However, wind turbines are not a well-applicable way of implementing the energy harvesting unit because of their low reliability. The wind turbines are usually implemented using a small brushed DC motor, which consists of moving parts. Components such as the shaft, gears, bearings, brushes and, to increase efficiency, a yaw system are continuously moving. These moving components tend to wear down easily and eventually cause a malfunction of the turbine. As a result of the lack of reliability, there is a significantly higher need for labour to maintain the availability of the system. On top of this, the fruit trees can become dominant obstacles in the operation of the turbine, which can significantly decrease the availability of the harvesting unit. Since this is in violation with requirements G1, G6 and G20, a wind turbine is disregarded as energy harvester.

3.2.2 Performance evaluation RF energy

To find the energy that can be harvested using an RF energy harvester, the minimum power requirements of the sensor node should be known first. According to requirements E5 and E6, the minimum power requirement is 3.31 μW + 5.28 μW = 8.59 μW or -20.7 dBm. This requirement indicates the minimal energy consumption of the microcontroller and wireless communication module when no data is transmitted. For RF energy harvesting this means that with an efficiency 30%, as indicated in Table 3.1, the continuous incident power must be higher than -15.43 dBm.

Single transmitting source

An estimation of the maximum distance that can be achieved to meet the minimum power requirements is made for the RF energy harvester as proposed by Parks [21], which was concluded as the best RF harvester implementation. This is done with the aid of Friis' formula, shown in Equation 3.2. In this equation P_t is the transmitted power, G_t is the gain of the transmitting antenna, G_r is the gain of the receiving antenna, and R the distance between the sender and receiver.

$$P_r = P_t \cdot G_t \cdot G_r \cdot (\frac{\lambda}{4\pi R})^2 \tag{3.2}$$

It was found by using the antenna register [22] that most GSM antennas have a transmit power of around 34.77dB if they are modelled as an isotropic antenna, and this value is used for $P_t \cdot G_t$. The minimum power requirement for the RF harvester is used for P_r, which equals -15.43 dBm. The gain G_r of the antenna of Parks is 6 dBi. The distance estimation is done for two different frequency bands used in the Netherlands. The first frequency band is from digital television broadcast which is in between 470 MHz until 700 MHz [23] and is shown in the left graph of Figure 3.2. The other frequency band is the lowest GSM frequency band which is between 800 MHz until 1000 MHz [24], and is shown in the right graph of Figure 3.2. In Appendix C.1 this distance is shown for the remaining higher GSM frequency bands used in the Netherlands.

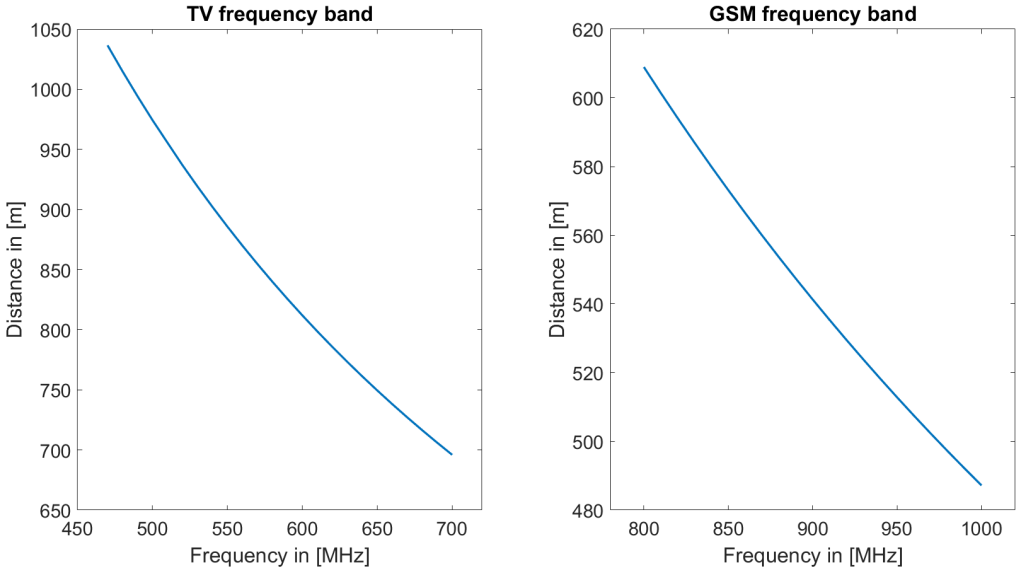

Figure 3.2: The maximum distance the RF energy harvester of Parks [21] can be located from a transmitting source to harvest -15.43 dBm as a function of frequency. This is done for the frequency band of digital television, shown in the left graph, and for the 800 MHz - 1000 MHz GSM frequency band, shown in the right graph.

The maximum distance the RF energy harvester can be placed from the source decreases for an increasing frequency. In the best case, the RF energy harvester can be placed at a distance of 1037 m from a digital television tower, and for the GSM band at best at 609 m. For the remaining higher GSM frequency bands the maximum distance the energy harvester can be placed becomes even lower, as visible in Appendix C.1. It can be concluded that the frequencies that can be used to harvest RF energy is limited by the distance the RF energy harvester is placed from the transmitting antenna, and can be 1037 m at best.

Multiple transmitting sources

The previous analysis only takes into account one transmitting antenna whereas in a practical situation multiple sources are transmitting simultaneously [22]. By using the superposition principle and Friis' formula on a set of antennas, each radiating at a certain frequency between 800 MHz and 955 MHz, the ambient RF energy distribution is found. To explore whether the ambient RF energy in a fruit orchard is

high enough to preserve the minimum power requirements of the sensor nodes, a test location of an agricultural area is selected in Flevoland. This province is chosen because it holds some of the largest fruit manufacturing companies in the country [25]. A map of this location together with the antennas considered is provided in Appendix C.2. The properties of these antennas are also provided in this appendix.

The result of the simulation is given in Figure 3.3. Both plots show the harvested power at each location in dBm by again using the RF harvester of Parks. From this figure can be concluded that for most of the land between the antennas, the ambient RF energy that can be harvested is around -20 dBm. The sensor nodes need at least -15.41 dBm of incoming power to operate, and therefore can not harvest enough energy in most of the field. Only at very small distances of a transmitting tower enough energy can be harvested, and the fact that multiple transmitting antennas are present does not increase the maximum range the RF energy harvester can be placed from a transmitting tower. This example indicates that it is not possible to use RF energy as the main ambient energy source for the energy harvesting unit because of the low power density of ambient RF energy present in a typical fruit orchard.

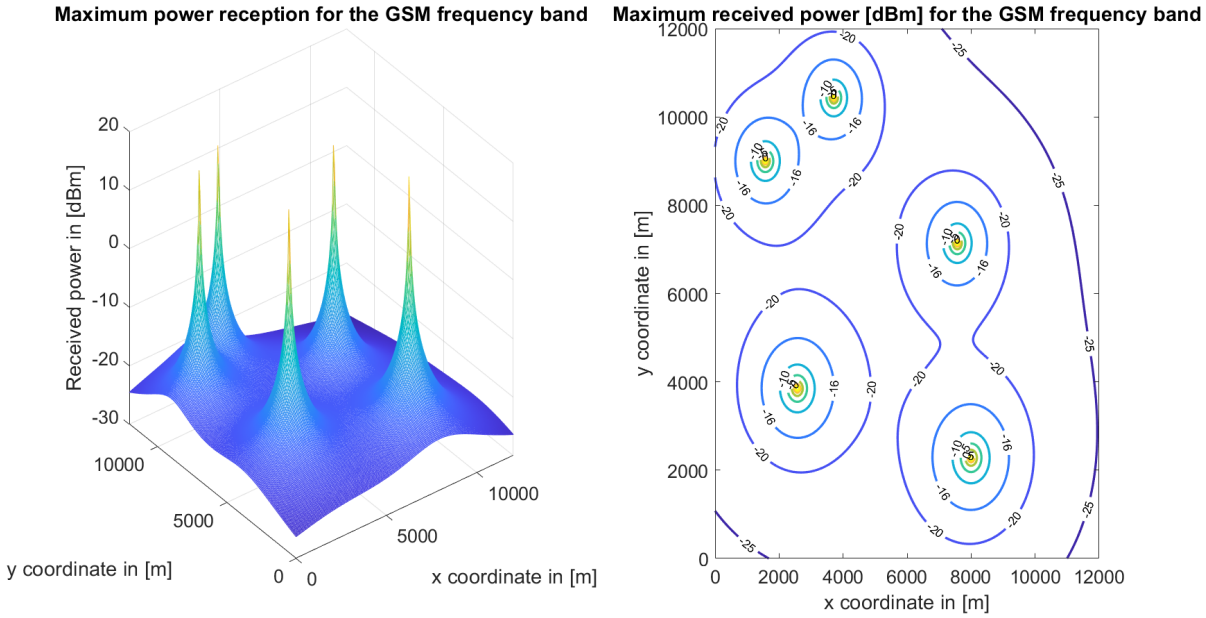

Figure 3.3: Distribution of the ambient Rf energy in dBm that can be harvested by an RF harvester that uses an antenna with a gain of 6 dBi. The distribution is the result of the 5 transmitting antennas as given in Appendix C.2.

3.2.3 Performance evaluation solar energy

It was found that neither wind energy, thermal energy nor RF energy are an adequate choice for the ambient energy source of the sensor node. By looking again at the minimum daily energy consumption, which is 8.59 μW, the minimum required peak power of the solar cell is found to sustain this consumption. For a solar cell with a harvesting efficiency of 30% this means that the peak power should be at least $8.59\ \mu W \cdot 24/(0.3 * 2.7) = 0.255\ mWp$ in order to satisfy the minimum power requirement. In contrast to RF energy, which is not able to sustain this minimum power requirement, solar energy is able to sustain this. Since solar energy also resulted as the best option in Table 3.2, solar energy is used as the ambient energy source to power the sensor nodes. In the next chapter, an in-depth analysis is done to find the solar cell that can sustain all power requirements.

Chapter 4

Energy harvesting

In the previous chapter is explained that solar energy is the most suitable ambient energy source for the energy harvesting module of the sensor nodes. In this chapter, the focus is put on the implementation of the energy harvesting module. First, the performance parameters of the solar cell are analysed, based on the energy requirements. Second, a choice is made about which solar cell is used for the implementation. Third, the solar cell control module is discussed. This module is first implemented using a simple implementing scheme after which it is compared with more complex maximum power point tracking (MPPT) implementations. Therefore, at the end of this chapter, the energy harvesting module is completely implemented.

4.1 Solar cell

Since the ambient solar energy is the only energy source that is used to power the sensor nodes, it is important that the solar cell can completely sustain the energy demand of the wireless communication module, temperature sensors, and the microcontroller. The power delivery capabilities of a solar cell are directly related to the size and conversion efficiency of the cell and are therefore important system parameters. In general, the type of solar cell largely affects the harvesting efficiency and is therefore also of importance. The power delivery capabilities of a solar cell are generally defined as the peak power under STC. This parameter takes both the conversion efficiency and size of the cell into account.

It is important to match the peak power of the cell with the energy demand of the node, since a too high peak power may result in overproduction and waste of resources, while a too low peak power may result in under production and so a loss of operation and availability. The challenge is to find the optimal size of the solar cell such that it satisfies requirements G6, G11, G20, and G23.

4.1.1 Solar cell power requirement analysis

In order to find the optimal sized solar cell for the energy harvesting unit, the peak power of the cell must be matched to the energy demand of the sensor node. Therefore, first the energy consumption of the sensor node is considered. For the energy consumption requirements E5, E6 and E7 are of importance, as well as the full top-level energy breakdown, which is provided in Appendix A.3. The requirements indicate the worst-case continuous power consumption of the microcontroller, temperature sensors and wireless communication unit. The total worst-case average continuous power consumption is given in Equation 4.1. On top of this, each transmission requires a worst-case energy consumption of 13.80 μWh in order for the wireless communication unit to send and receive a data packet.

$$P = P_{wireless} + P_{temperature} + P_{microcontroller} = 5.28\mu W + 0.9\mu W + 2.406\mu W = 8.59\mu W \tag{4.1}$$

Using these constraints of energy requirements, the average daily energy consumption is found. The daily energy consumption is heavily influenced by the temperature, so weather data is used to analyse this. By making use of the past 10 years of hourly temperature data, from February 2009 till June 2019 station 269 Lelystad, an estimate is made of the energy usage of the sensor node [26]. Figure 4.1 shows the energy consumption of a sensor node when it operates in normal operation mode, using the 10 years of hourly temperature data. The normal operation mode of the sensor is further explained in Appendix A.2.

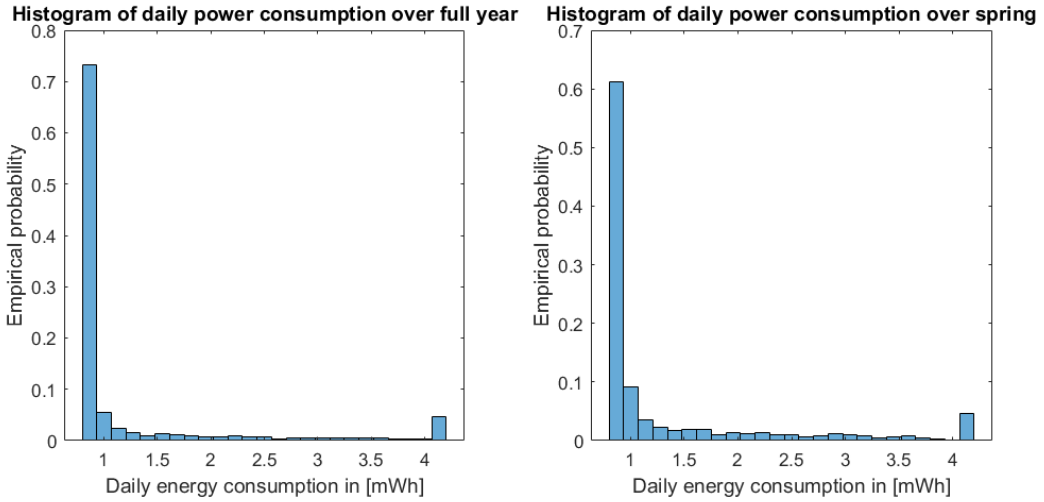

Figure 4.1: Histograms of the daily energy consumption of the sensor node when it operates in normal operation mode. The left graph shows the result using the temperature data from February 2009 up to June 2019. The right figure shows the result using the temperature data of the spring months only, which are February March April and May, for the years 2009 up to and including 2019.

The left graph of Figure 4.1 shows a histogram of the energy consumption of a sensor node when the temperature data of the full years is used, whereas the right figure displays a histogram based on only the spring temperature data, from February till June. As stated by requirement G23, the spring months are of most importance for the sensor nodes and so the energy consumption in the right figure is taken into account. This figure indicates that during spring the average daily energy consumption is 1.34 mWh and the maximum consumption is 4.18 mWh. The figure also indicates that the empirical probability of having this maximum energy consumption is 0.05. Since this probability is quite significant, the minimal daily energy requirements are set at the worst case of 4.18 mWh per day.

Using these energy requirements of the sensor nodes, an estimate can be made for the minimal required peak power of the solar cell. To obtain the required peak power, a simulation is used based on the past 10 years of hourly temperature and irradiance data, from February till June in years 2009-2019 at station 269 Lelystad [26]. This simulation makes use of several assumptions:

A1. A constant conversion efficiency of the solar cell is assumed. This means that the harvesting efficiency of the solar cell is not influenced by the amount of incoming solar irradiance. Chegaar et al. [27] states that the efficiency of the solar cell varies little with the illumination intensity, so the assumption is plausible.

A2. An illumination intensity of 81% of the measured irradiance data is used as input of the solar cell. This factor is a result of the fixed placement of the solar cell. Even though the optimal placement is used as mentioned in Appendix B.1.2, the orientation of the solar cell is fixed throughout the day. The irradiation data is however orientation independent, so is on average higher than the real incoming power. According to Edinbarough [28] and Nagy et al. [29], using a solar tracker system can increase the harvesting efficiency of the solar cell by 24%-25%. In that case maximum solar energy is harvested, so the conversion factor of 1/1.24 = 0.81 is used on the solar irradiance data.

A3. To make an estimate of the required peak power of the solar cell, only daily power consumption is assumed to be of importance. The cell size is chosen such that it matches the daily power requirements and neglects the remainder of the energy harvested in the previous day.

The result of the simulation is shown in Figure 4.2. This figure shows the required peak power of the solar cell when using the hourly temperature and irradiance data. For the energy consumption of the sensor node, it is assumed that the node operates in normal operation mode. From the simulation can be concluded that the average required peak power of the solar cell is 2.89 mWp. The maximum required peak power is 25.0 mWp.

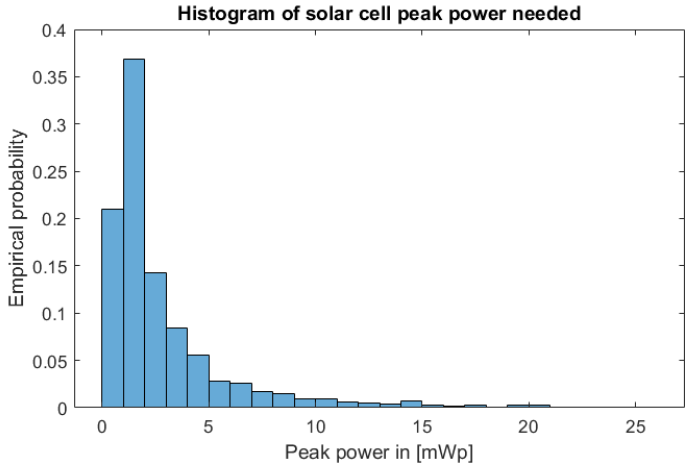

Figure 4.2: Histogram of the minimal required peak power of the solar cell based on hourly irradiation and daily energy consumption of the sensor node.

Now if a solar cell with a peak power of 20 mWp is chosen as the implementation, the daily power delivery can be lower than the power consumed that day. Figure 4.3 shows the net produced energy of a sensor node at the end of a day. It can be concluded that with a 20 mWp solar cell, the probability to not meet the daily power requirements is 0.002 and the worst case is energy shortage is 0.85 mWh. However, the average daily surplus of energy is 51.99 mWh, so the shortage of energy can be solved with an energy storage unit that can store energy for more than a day, as stated by requirement E10.

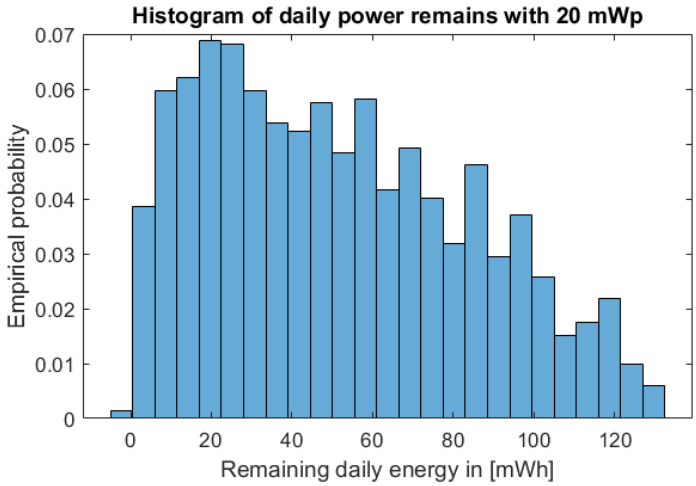

Figure 4.3: Histogram of daily energy surplus of the sensor node, based on hourly irradiation and daily energy consumption.

So according to the simulations a solar cell of 20 mWp would be sufficient to meet the power needs of the sensor nodes, thereby satisfying requirements E5, E6, E7. However, during the simulations some assumptions are taken into account. Besides, the inefficiencies of the control module, energy monitoring and energy storage are not taken into account yet. To make sure that with these inefficiencies the system can still be operated, the solar cell must be chosen larger than 20 mWp.

4.1.2 Solar cell specifications

There are three main types of solar cells available, which are monocrystalline, polycrystalline and amorphous silicon. In table 4.1 the typical conversion efficiency, price per Wp and applications are listed for these types of cells. The most interesting type of cell is monocrystalline silicon since it has the highest conversion efficiency.

Table 4.1: Overview of different types of often used solar cells [30] [31] [15].

Solar cell type	Conversion efficiency	Price per Wp	Typical application
Monocrystalline silicon	17%-25%	€0.51 - €0.63	Large scale harvesting
Polycrystalline silicon	13%-17%	€0.44 - € 0.63	Large scale harvesting
Amorphous silicon	6%-7%	-	Calculators

Table D.1 given in Appendix D gives a selection of solar cells and their properties that are suitable for the application. The selection of solar cells is made based on the properties of the MPPT module, and the minimum peak power requirement as mentioned before in Section 4.1.1. The MPPT module used is the SPV1050, this choice of control module is later explained in Section 4.2.3. To come to a structured choice, the solar cells are weighted against each other on different criteria, which is described below.

Power delivery

The power delivery is the maximum peak power that can be harvested with the solar cell. This is regarded as the most important criterion since this limits the total power that can be harvested each day. This, in turn, limits the maximum power consumption of the sensor node. From the selection, the SM500K12L has the highest peak power that can be harvested while having approximately the same size as the other solar cells. Also, having a maximum peak power of 132.3 mW can significantly improve the probability that enough energy can be harvested each day.

Efficiency

The efficiency of a solar cell is the conversion efficiency of the incoming radiation into electrical energy and is therefore an important parameter. Normally this differs per solar cell, but in this case they all have an efficiency of 25%. The efficiency is constant, because the selected solar cells are from the same series and made by the same manufacturer. This is the only manufacturer considered, as it is specialised in small and reliable solar cells. Therefore this criterion is not taken into account in the selection of solar cells.

Typical MPP current

The typical MPP current is the current that is delivered by the solar cell at its MPP. This criterion is regarded as the second most important, since the efficiency of the SPV1050 strongly depends on the current supplied by the solar cell. This current should not be higher than 20 mA, since the datasheet of the SPV1050 does not mention the maximum input current or power, and displays its efficiency characteristic up to an input current of 20 mA [32]. Since no measurements can be done to see if a higher input current is supported and what the corresponding efficiency characteristic is, a value of 20 mA is taken as a limit. The SPV1050 is used in a buck-boost configuration. At 3 mA the efficiency of the module in this configuration is the highest and is therefore the optimal MPP current. The SM240K10L has an input current of 13.2 mA, which is the closest to the optimum current of 3 mA and scores the highest, while the SM500K12L has an input current of 19.8 mA, which scores the lowest.

Open circuit voltage

The open-circuit voltage of the solar cell should be in between 6 V and 18 V. The datasheet of the SPV1050 does not show its efficiency characteristics in buck-boost configuration for an open circuit voltage less than 6 V. Since no experiments can be done to measure the efficiency characteristics for lower voltages, this voltage is chosen as the lower threshold. This criterion is regarded less important than the typical MPP current since the efficiency of the SPV1050 does not depend strongly on the open circuit voltage, as is the case with the MPP current. If the storage unit is fully charged, the open-circuit voltage is imposed on the input terminal of the SPV1050. Since the maximum rating is 18 V, the open-circuit voltage of the solar cell should not exceed this. The open-circuit voltage should be close to 9 V, because the efficiency curves in the datasheet of the SPV1050 show the least dependence on the input current at this voltage, and is almost maximum for a large range of input currents. Moreover, the highest efficiency in the buck-boost configuration can be achieved for this open circuit voltage, which is approximately 84%. The SM500K12L and SM470K12L both score the highest since they have an open-circuit voltage of 8.29 V. The SM400K10L and the SM340K10L both have an open circuit voltage of 6.91 V and therefore score lower.

Price

The price of the solar cell should be kept as low as possible. According to requirement G14 and G21 the total number of solar cells on an average fruit orchard will be 1000 solar cells, so a small decrease in the cost of a solar cell will reduce the total cost of the sensor network significantly. However, the price is not a very important criterion as the main goal for the solar cell is to satisfy requirement G6, and not minimising the cost. The SM500K12L is the most expensive solar cell and scores the lowest, while the SM340K10L is the cheapest and scores the highest. Note that no price of the SM470K12L is given since it is currently not widely available on the market.

Size

Finally, the size of the solar cell should be considered, since the solar cell has to fit on the pole. However, since the sizes of the selected solar cells do not differ much and all fit on the pole, this criterion is regarded as the least important. The SM340K10L and SM400K10L are approximately the same size and are the smallest of the selected solar cells. The SM500K12L and the SM470K12L are also approximately the same size and are slightly larger than the other two solar cells.

Final decision

A comparison table is made according to the previous comparison in order to select the optimal solar cell, and is listed in Table 4.2. Each criterion is given a weight from 1 to 10 based on its importance, where 10 is the most important. The different solar cells are then given a score from 1 to 10 for each criterion, where 10 is the best. The highest total weighted sum of the score then gives an indication of the most suitable option.

Table 4.2: Comparison table of the suitable solar cells.

		SM500K12L		**SM400K10L**		**SM470K12L**		**SM340K10L**	
Criterion	**Weight**	**Score**	**Weighted**	**Score**	**Weighted**	**Score**	**Weighted**	**Score**	**Weighted**
Power delivery	9	10	90	7	63	9	81	6	54
Typical MPP current	8	6	48	7	56	6	48	8	64
Open circuit voltage	7	9	63	6	42	9	63	6	42
Price	4	6	24	7	28	0	0	8	32
Size	2	7	14	8	16	7	14	8	16
			239		205		206		208

From the scores in the table can be concluded that the SM500K12L is the most suitable solar cell. This solar cell is used for the project, because it has the highest maximum peak power, and because the open circuit voltage is close to the ideal 9 V. The SM470K12L is the only solar cell that is similar to the chosen SM500K12L, but since it is currently not widely available on the market and has a slightly lower maximum peak power, it is not chosen.

4.2 Solar cell control module

The solar cell cannot be directly connected to the storage unit and needs some sort of control module. Without a control module, the storage unit discharges itself over the solar cell when the solar cell is not subjected to enough irradiance. This happens mostly during the night and dark days. Also, the harvesting efficiency of the energy module can be improved when using a control module. This module is first implemented using a simple implementing scheme, after which it is compared with maximum power point tracking implementations.

4.2.1 Single diode

The most simple implementation of the control module is placing a diode in between the solar cell and the storage unit. In Figure 4.4 the schematic of this implementation is shown. Note that the storage unit is implemented as a supercapacitor, see Chapter 5 for this decision. With this implementation, the supercapacitor does not discharge over the solar panel when the solar cell does not produce energy, only the leakage current of the diode remains.

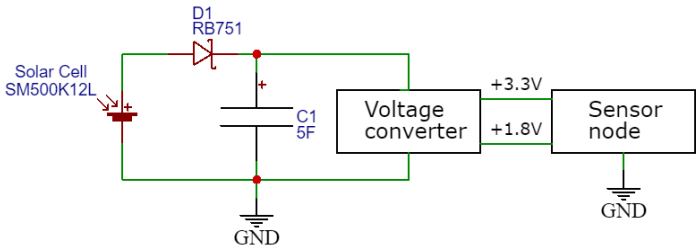

Figure 4.4: Schematic of the single diode implementation to charge the supercapacitor.

The diode used is the Vishay RB751 Schottky diode. This diode is chosen for its low forward voltage drop of 0.5 V at a current of 20 mA, and for its low leakage current of 20 nA at a reverse voltage of 10 V [33]. Simulations have been done to verify that this implementation can be used and to obtain the efficiency of this implementation. In Appendix E.2 the simulation model used is elaborated.

The simulation is done for different values of incoming solar irradiance Ir at a temperature of 25 °C. In Figure 4.5 the power flowing into the supercapacitor over time is shown for different irradiances, where the supercapacitor is initially discharged. Each irradiance curve has only one peak. This can be explained by the fact that the voltage V_{C1} of the supercapacitor increases as it charges. When V_{D1} is the voltage over the diode, the voltage over the solar cell is $V_{C1} + V_{D1}$. At a peak, the voltage over the solar cell reaches the MPP voltage, thus maximum power is harvested and delivered to the supercapacitor. Further, the time required for the supercapacitor to fully charge increases for lower irradiances, since the maximum power that can be harvested is proportional to the irradiance.

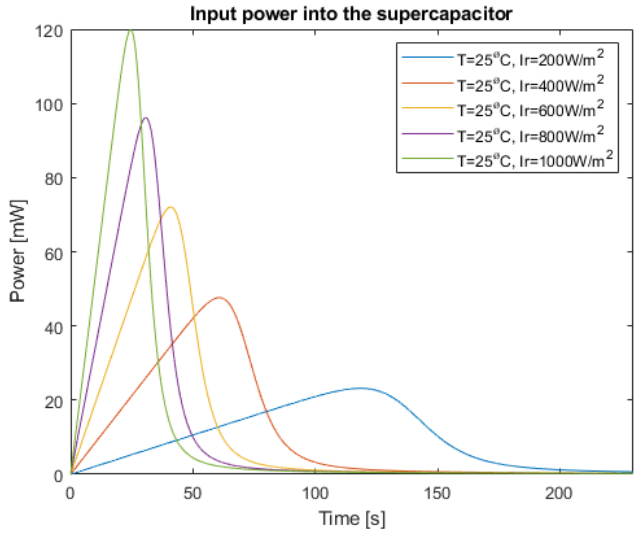

Figure 4.5: Simulated power flowing into the supercapacitor as a function of time, using a diode as control unit.

The efficiency during charging as a function of the supercapacitor voltage is shown in Figure 4.6. Applying assumption A1, the efficiency is calculated using Equation 4.2, where $P_{Ir}(V)$ is the power flowing into the supercapacitor as function of the supercapacitor voltage for an irradiance intensity Ir, $P_{MPP,Ir}$ is the MPP power for an irradiance intensity Ir, and P_{MPP} is the MPP for STC which equals 132.3 mW for the solar cell used.

$$\eta = \frac{P_{Ir}(V)}{P_{MPP,Ir}} = \frac{1000 P_{Ir}(V)}{Ir \cdot P_{MPP}} \tag{4.2}$$

In Figure 4.6 is shown that the efficiency is maximum at the MPP voltage only. For lower irradiances, the MPP voltage decreases slightly, and less efficiency can be achieved at MPP. The efficiency drops fast when the voltage of the supercapacitor approaches V_{oc} of the solar panel, which means that the last part

to fully charge the capacitor to V_{oc} takes a relatively long time. This can also be seen in Figure 4.5. After the MPP, the power drops fast, and it takes a relatively long time for the curves to reach zero. Note that the supercapacitor should have a rated voltage higher than V_{oc} for this implementation. Furthermore, the efficiency is low if the capacitor has a low voltage, which is the case if the supercapacitor has little energy left. Finally, the efficiency is always lower than 100% because power is dissipated in the diode due to the forward voltage drop of $V_{D1} = 0.5V$. At MPP at STC, a power P_{D1} of 9.9 mW is dissipated in the diode, and a maximum efficiency of

$$\eta = \frac{P_{D1}}{P_{MPP}} \cdot 100\% = 92.52\%$$

can be achieved.

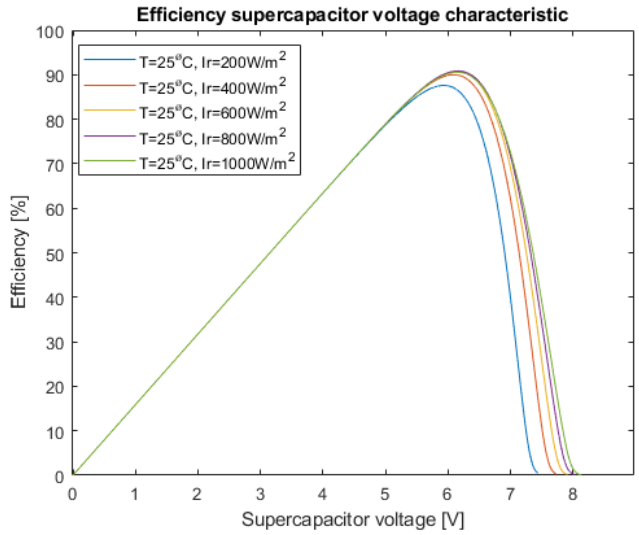

Figure 4.6: Simulated efficiency of charging the supercapacitor as a function of the supercapacitor voltage, using a diode as control unit.

4.2.2 Maximum Power Point Tracking

As can be concluded from the simulations of the diode implementation, there are two main drawbacks. First, the loss of harvesting efficiency due to the non-ideal operation point of the solar cell and second, the lower efficiency of conversion due to the dissipation of energy in the diode. In order to solve these two drawbacks, a more complex implementation of the control module is used. The first problem can be solved by using a maximum power point tracking module. This module, introduced in Appendix B.1.1, is used to maximise the harvesting efficiency of the solar cell by optimising its operating conditions. From Figure E.3 in Appendix E can be concluded that the maximum power of the solar cell is delivered if the voltage across its terminals is between 6.4 V and 7.0 V. This, at all times, corresponds to around 84% of the open-circuit voltage, independent of the irradiance. An MPPT module then uses an algorithm to find this voltage at which the power delivery is maximised and set it across the terminals of the solar cell.

The MPPT modules that are considered, together with their specifications, are presented in Table D.2 which is given in Appendix D. To make a choice which control module is best suited for the implementation of the energy harvesting system, requirements E1 up to E4 and the specifications of the SM500K12L solar cell are of importance. To come to a structured choice, the MPPT modules are weighted against each other on different criteria, which are described below.

Operation voltage input

The first criterion is the input operation voltage, which takes into account the voltage range of input and the cold-start voltage. When the input range is large, more solar cells can be used. So the control module with the largest input voltage range, the SPV1050, gets a higher score. Also, the cold start voltage is important, because this defines the threshold voltage the solar cell must reach in order to activate the harvesting. The control module with the lowest cold-start voltage, the LTC3105, gets a higher score. As can be concluded

from Table 4.3, the SPV1050 gets the highest score partly because it meets the input range requirements of 0 V to 8.29 V from the chosen solar cell.

Maximum storage voltage

The second criterion that is of importance is the maximum voltage that can be achieved over the energy storage unit. The energy stored in the storage unit, as is explained in Chapter 5, is quadratically proportional with the potential across the storage units terminals. To guarantee continuity of the power supply, the energy storage must be sufficiently large. Therefore to satisfy requirement E10, a large voltage across the storage terminals is important. This criterion is seen as the most important one since it largely affects the later design of the storage unit. The LTC3129 has the highest output voltage range up to 15.7 V, so gets the highest score. In contrast, the AEM10941 has a storage voltage range of 4.5 V, so gets the lowest score.

Quiescent current

The third criterion is the quiescent current. This measure is composed of two components. The first component is the quiescent current in operation mode, which is the current the energy harvesting module needs in order to perform the MPPT operation. This is the lowest for the BQ22504 and BQ25570, while in contrast, the LTC3105 has a very high operational quiescent current. The second component is the standby-quiescent current, which is consumed if no energy is harvested. This current is the lowest for the SPV1050.

Efficiency of harvesting

The efficiency of harvesting provides the rate of efficiency at which the energy harvested by the solar cell is converted into energy at the output of the control module. This efficiency should be as high as possible to guarantee proper conversion of the harvested energy and low overhead solar cell size. The highest efficiency is obtained when using the AEM10941, which has a conversion efficiency of up to 96%. The lowest efficiency is obtained when using the LTC3105, which gets the lowest score.

Output characteristics

Another important criterion is the output characteristics. As was mentioned in requirements E1 and E2, the microcontroller should have its power supplied at a potential of 1.8V, whereas the wireless communication module should operate at 3.3V. Requirements E3 and E4 indicate the peak power consumption of the two modules. The wireless communication module and microcontroller unit require a peak current of 36.50 mA and 7.92 mA respectively. The controller module with the best output characteristics is the SPV1050, this module has two low dropout regulators (LDOs) of 1.8 V and 3.3 V that can supply each up to 200 mA. In contrast, the AEM10941, BQ25570, BQ25504, and LTC3105 all have only one variable output terminal. One external LDO regulator must be implemented when one of these modules is used. Morevover, the LTC3105 can only supply up to 12 mA from this LDO, and therefore scores low. The LTC3129 does not contain any output regulator, so scores the lowest.

Price

The price of the implementation is of importance and must be kept as low as possible to reduce the overall cost of the sensor node. The cost of the SPV1050 is €1.36 if bought in bulk, which is low compared to the other modules. The AEM10941 has the highest price, at €4.00 if bought in bulk. Therefore, the SPV1050 gets the highest score.

Implementation difficulty

The last criterion is the implementation difficulty. This parameter gives an indication of the amount of work needed to implement the module. In the case of the LTC3129, no energy distributing control module is included. The flow of power from the storage module to the microcontroller, temperature sensors, and wireless communication module, as well as the conversion of the power properties of the output must be done by external components. Also, the lack of data in the datasheet of the LTC3129 causes the score to be low.

Final decision

Table 4.3 concludes the allocation of the scores to the different criteria for each of the MPPT module. Each criterion is given a weight from 1 to 10 based on its importance. The different MPPT modules are then given a score from 1 to 10 for each criterion. The highest total weighted sum of the score then gives an indication of the most suitable option.

Table 4.3: Comparison table of the suitable MPPT control module.

		SPV1050		**AEM10941**		**BQ25570**	
Criterion	**Weights**	**Score**	**Weighted**	**Score**	**Weighted**	**Score**	**Weighted**
Operation voltage input	3	10	30	6	18	6	18
Peak storage voltage	9	7	63	5	45	8	72
Quiescent current	5	6	30	7	35	8	40
Efficiency of harvesting	4	6	24	9	36	7	28
Output characteristics	7	9	63	8	56	6	42
Price	2	10	20	6	12	7	14
Implementation difficulty	6	9	54	9	54	7	42
			284		256		256

		BQ25504		**LTC3105**		**LTC3129**	
Criterion	**Weights**	**Score**	**Weighted**	**Score**	**Weighted**	**Score**	**Weighted**
Operation voltage input	3	3	9	7	21	8	24
Peak storage voltage	9	6	54	7	63	10	90
Quiescent current	5	9	45	2	10	7	35
Efficiency of harvesting	4	6	24	5	20	8	32
Output characteristics	7	6	42	3	21	1	7
Price	2	9	18	7	14	8	16
Implementation difficulty	6	6	36	5	30	1	6
			228		179		210

From Table 4.3 can be concluded that the most optimal maximum power point tracking module is the SPV1050. This module has obtained the highest score of all the control modules because of its output characteristics, low price, and mainly because its wide input voltage range that fit the remaining design of the sensor node. Therefore the SPV1050 is the MPPT module of choice.

4.2.3 Choice of control module

The advantages of the single diode implementation are its simplicity and low cost. However, the disadvantages outweigh the advantages. The charging efficiency as well as the power harvesting cannot be controlled and are only optimum at a single supercapacitor voltage. When the supercapacitor is depleted, the power harvested is minimal. Also, charging to the maximum voltage takes a long time. Further, there will always be a voltage drop over the diode when the solar cell harvests energy, and when the solar cell does not harvest energy there is always a leakage current. Finally, two regulators to supply the correct voltages to the remaining sensor node are still needed.

The main advantage of the SPV1050 MPPT module over the diode implementation is that it solves these two problems. The harvesting efficiency is high, up to 84%, and almost independent of the capacitor voltage. Also, the module has two built-in LDO regulators at 1.8 V and 3.3 V. Finally, the control module has the ability to control the incoming and outgoing power such that minimum energy gets lost when the solar cell is not producing any power, making long term energy storage possible. Overall the design of the control module using the SPV1050 has much more advantages that outweigh the extra higher price of the module compared to the diode implementation. Therefore, the SPV1050 is used as the main energy harvesting control module.

Chapter 5

Energy Storage

In the previous chapter, the energy module was designed from an energy harvesting perspective. The SPV1050 was chosen as the main control module of the energy system. In this chapter, the focus is set on finding the implementation of the energy storage unit, which is used to create continuity of energy supply to the sensor node. The chapter starts with defining the different types of storage implementations and goes further into explaining the specifications and choice of the energy storage module. Finally, also the energy monitoring circuit is designed and simulated.

5.1 Types of energy storage

For the implementation of the energy storage module two types of storage units can be used, which are the rechargeable battery and the supercapacitor. There are four main types of rechargeable batteries available, which are lead-acid, nickel-cadmium (NiCad), nickel-metal-hydride (NiMH), and lithium-ion (Li-ion) [34]. Batteries have the advantage over supercapacitors that their energy densities are much higher. Also, they can store the energy for longer periods, because of their low leakage current. However, batteries have a limited amount of charge-discharge cycles. Lithium-ion has the highest cycle life with 2000 cycles, which corresponds to a maximum of five and a half years when it is cycled each day with 80% depth of discharge (DoD) [34]. After this time they need to be replaced, and since this conflicts with requirements G20 and E9, rechargeable batteries are not suitable for this project.

For supercapacitors, three types can be distinguished, which are Electric Double Layer Capacitors (EDLC), pseudocapacitors, and hybrid capacitors. EDLCs are widely available for all kinds of capacitances ranging from a few millifarads to thousands of farads and have a cycle life between 50000 and 500000 cycles. A large drawback of the supercapacitors is that they have a high self-discharge rate, so stored energy is internally dissipated, causing an increase in the overall energy consumption.

Pseudocapacitors and hybrid capacitors are a type of electrochemical capacitors that can store more energy due to the usage of chemical bonds, just as in batteries. Therefore they have properties from both capacitors and batteries. They have a higher power density and lower self-discharge rate than capacitors, and they can support higher charge and discharge currents than batteries, as well as a much longer cycle life of around 50000 cycles [35]. However, pseudocapacitors suffer from having a low capacitance, and their performance deteriorates due to faradic redox reactions [36]. Furthermore, they are not readily available on the market.

Hybrid capacitors are more readily available in combination with lithium-ion. However, the maximum rated voltage does not exceed 3.8 V for any of the available brands. This is quite low since the minimum voltage of the storage should be 3.3 V for the SPV1050 to power the wireless communication module. Furthermore, there is very limited information provided in the datasheets of the hybrid capacitors. Just as in Li-ion batteries, there is no clearly defined relationship between the energy left in the Li-ion capacitor and the voltage of this capacitor. Since this information lacks in all datasheets, no accurate estimation can be done to see if enough energy is available before the voltage drops below 3.3 V, and therefore this storage is disregarded.

5.2 Implementation energy storage

As can be concluded from the previous section, rechargeable batteries are not seen as a viable solution, as well as pseudocapacitors and hybrid capacitors. An EDLC, on the contrary, can be used with the SPV1050

and complies to requirements G7, G20, and E9. The energy storage unit is therefore implemented using an EDLC. The main drawback of this implementation is that it has a high self-discharge rate. To comply with requirements G11 and E10, an EDLC is chosen such that it can store enough energy to meet the power requirements while taking the large leakage current into account. For supercapacitors generally holds that a larger capacitance can store more energy but have a higher leakage current. Therefore, a trade-off is made between the size of the supercapacitor and the associated leakage current of the supercapacitor.

To determine the supercapacitor that is used for the implementation of the energy storage module, a set of suitable supercapacitors is chosen and is listed with their properties in Table D.3 in Appendix D. The supercapacitor, when implemented, is connected to the SPV1050. Because of the properties of this module, the EDLC can properly operate in the energy range of 3.3 V until 5.3 V. Otherwise, the wireless communication unit can not be powered by the SPV1050. Using this limited voltage range, the usable energy that can be stored in the supercapacitor is calculated using Equation 5.1.

$$E = \frac{1}{2}C(5.3^2 - 3.3^2) \tag{5.1}$$

To take into account both the rated capacitance and the leakage characteristics of the supercapacitor, the average operation time of the supercapacitor is found. This is the time to go from a full 5.3 V EDLC to a functionally empty 3.3 V EDLC if an average energy consumption of 1.34 mWh is used, as introduced in Section 4.1.1. Also, an additional loss of 0.40 mWh is taken into account for the the energy control module and the energy level monitoring circuit, see Chapter 5.3. Finally also, the corresponding leakage current of the supercapacitors is taken into account. Figure 5.1 indicates the average operation time of the selected supercapacitors against their price of investment. The best supercapacitors are present in the top left of the figure.

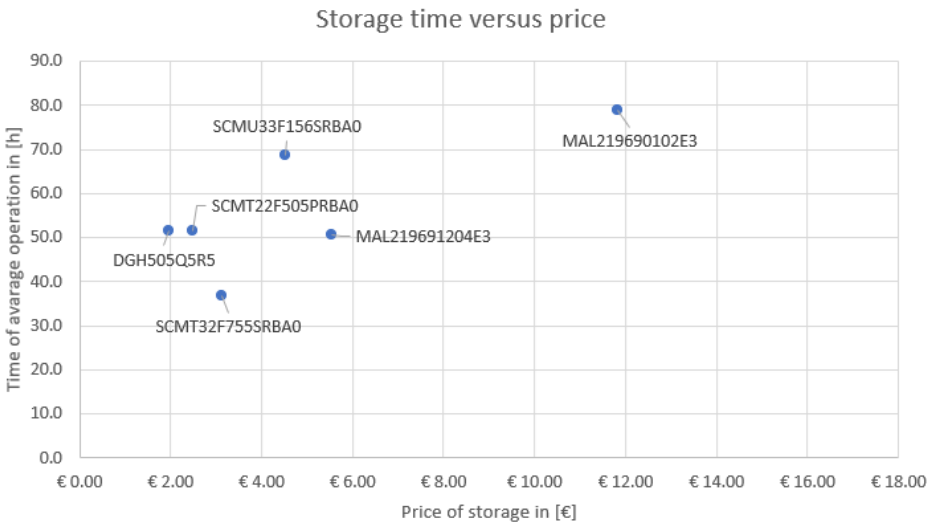

Figure 5.1: Scatter plot of the possible energy storage unit implementations, representing the price against the estimated time the sensor node can operate under average operation conditions without incoming energy from the energy source.

To make a choice which EDLC is best suited for the implementation of the energy storage unit, requirements G11 and E10, and the properties of the SPV1050 are of importance. To come to a structured choice, the supercapacitors are assigned a score on different criteria. These scores are provided in Table 5.1 and are explained below.

Rated capacitance

The first important measure is the rated capacitance of the EDLC, which is a measure of the energy storage capability of the storage module. As indicated by Equation 5.1, a larger capacitance increases the energy that can be stored at a terminal voltage. To comply with requirements G11 and E10, the energy storage capacity should be large enough to guarantee the operation of the sensor after 2 days of no incoming

power. The MAL219691204E3 EDLC has the largest rated capacitance of 90 F and gets the highest score. In contrast, the SCMT22F505PRBA0 and DGH505Q5R5 have rated capacitances of 5 F and end up with the lowest score.

Leakage current

In addition to the size of the supercapacitor, the leakage current is an important measure. The leakage current of the supercapacitor causes the stored energy to be dissipated over time. Because of this leakage current, additional energy must be produced to overcome the losses, thus a larger storage unit is required to comply with requirements G11 and E10. As a result, the leakage current is seen as the most important criterion. The 5 F SCMT22F505PRBA0 has the lowest leakage current of 30 μA and therefore gets the highest score. The MAL219691204E3, as expected because of its large size, has the largest leakage current of 500 μA and scores the lowest.

DC ESR

The DC ESR is the equivalent series resistance of the supercapacitor if it is operated in DC conditions. The EDLC can then be seen as if it is a series connection of an ideal EDLC and a resistance. If the DC ESR has a large value, a significant part of the energy flowing in or out of the supercapacitor is dissipated in this resistance in terms of heat. A higher ESR reduces the round trip efficiency of the EDLC, so must be chosen as low as possible. However, only currents in the range of microamperes will flow and the effect of the ESR becomes less dominant. Therefore this criterion is regarded as the least important. The SCMU33F156SRBA0 has the lowest equivalent series resistance of 50 $m\Omega$ and gets the highest score. In contrast, the MAL219691204E3 has with a series resistance of 10 Ω the lowest score.

Price

The price of the supercapacitor is of importance since it must be kept as low as possible to reduce the overall cost of the system implementation. As the energy storage module is quite expensive, it significantly influences the price of the energy harvesting module as a whole. The 5 F DGH505Q5R5 supercapacitor is the cheapest implementation at the price of €1.95. Therefore, this EDLC gets the highest score. In contrast, the MAL219690102E is much more expensive, at the price of €11.83. As a result, this 90 F supercapacitor gets the lowest score.

Table 5.1: Comparison table of the suitable EDLCs.

		SCMT32F755SRBA0		SCMU33F156SRBA0		SCMT22F505PRBA0	
Comparison table	**Weights:**	**Score**	**Weighted**	**Score**	**Weighted**	**Score**	**Weighted**
Rated capacitance	7	7	49	8	56	6	42
Leakage current	9	6	54	6	54	8	72
DC ESR	4	8	32	10	40	5	20
Price	5	7	35	5	25	8	40
			170		175		174

		MAL219691204E3		MAL219690102E3		DGH505Q5R5	
Comparison table	**Weights:**	**Score**	**Weighted**	**Score**	**Weighted**	**Score**	**Weighted**
Rated capacitance	7	8	56	10	70	6	42
Leakage current	9	5	45	1	9	8	72
DC ESR	4	1	4	4	16	8	32
Price	5	4	20	1	5	9	45
			125		100		191

As can be concluded from Table 5.1, the DGH505Q5R5 is best suited for the implementation of the energy storage module. This supercapacitor has the best trade-off between energy storage, price, and leakage current, as indicated by Figure 5.1. The supercapacitor is the cheapest option from the selected EDLCs and is able to sustain the average power consumption of the sensor node for 51.6 hours. The functional energy storage of the DGH505Q5R5 is 11.94 mWh according to Equation 5.1. The same simulation as in Figure 4.3 is done with the SM500K12L solar cell instead of a 20 mWp solar cell. From this simulation is concluded that the average daily overproduction of the solar cell is 351 mWh, so the supercapacitor can be easily charged to full capacity. The implementation therefore satisfies requirements G7, G11, G20, E9 and E10.

5.3 Energy level monitoring

For the microcontroller to decide in which mode of operation it must operate, the amount of energy stored in the supercapacitor has to be known. As can be concluded from Equation 5.2, there is a quadratic relation between the terminal voltage across a supercapacitor and energy stored in that capacitor, thus a voltage monitoring system is designed.

$$E = \frac{1}{2}CV^2 \tag{5.2}$$

The voltage is measured using an analogue Input/Output (IO) pin of the Microcontroller Unit (MCU) from the microcontroller group [5]. This IO pin is connected to an Analog to Digital Converter (ADC) and has an input voltage range of 0 V up to 1.7 V. Therefore, a voltage divider is implemented to convert the maximum voltage of 5.3 V of the supercapacitor to 1.7 V at the IO pin. Furthermore, to reduce static power consumption, the monitoring system is normally disconnected from the supercapacitor and is only connected when a voltage measurement is required. This is done by using a control signal from the MCU.

To increase the measurement accuracy in the range of operation, a Zener diode can be placed between the supercapacitor and the voltage divider. However, this introduces non-linearities in the measured voltage at the MCU. Further, to reach the Zener voltage drop, a current in the order of milliamperes has to flow which results in more power loss. Moreover, the voltage can not be measured if the supercapacitor drops below the Zener voltage. Also, a sufficient accuracy can be obtained without a Zener diode, as explained in Section 5.3.1. Therefore, a Zener diode is disregarded from the implementation.

5.3.1 Design of energy monitoring circuit

The schematic of the supercapacitor energy monitoring system is shown in Figure 5.2. The resistors $R1$ and $R2$ form the voltage divider, and the voltage over $R2$ is measured by the MCU, indicated as MCU_level. The voltage V_{MCU_level} is calculated as

$$V_{MCU\_level} = \frac{R2}{R1 + R2}V_C$$

where V_C is the supercapacitor voltage. To obtain a maximum of 1.7 V at MCU_level, a factor of

$$\frac{R2}{R1 + R2} = \frac{1.7}{5.3}$$

is required. To limit the power consumption the resistor values should be high, but to limit the effect of thermal noise of the resistors on the measurements the resistor values should be low. A trade off is made which results in a restricted maximum current of 40 μA through $R1$ and $R2$. This requires a total resistance of

$$R_{eq} = \frac{V_{C,max}}{I_{max}} = \frac{5.3}{40 \cdot 10^{-6}} = 132.5\ k\Omega$$

where $R_{eq} = R1 + R2$. From this follows that

$$R2 = \frac{1.7}{5.3}R_{eq} = 42.5\ k\Omega$$

and

$$R1 = (1 - \frac{1.7}{5.3})R_{eq} = 90\ k\Omega$$

For $R1$ a value of 91 $k\Omega$ is used, and for $R2$ a value of 43 $k\Omega$ is used, since these are the closest common resistor values. The voltage of MCU_level is measured using a 12 bit ADC, which results in an accuracy of

$$\delta V = \frac{V_C, max}{2^{n+1}} = \frac{5.3}{2^{13}} \approx 646.97\ \mu V$$

This error is of most importance for the microcontroller to decide if a transmission can be done when the supercapacitor is almost depleted to 3.3 V. The error in energy level at 3.3 V is

$$\delta E = \frac{C \cdot (V_{C,3.3V}^2 - (V_{C,3.3V} - \delta V)^2)}{2 \cdot 3600} = \frac{15(3.3^2 - (3.3 - 646.97 \cdot 10^{-6})^2)}{7200} \approx 8.89\,\mu Wh$$

Since one transmission costs 13.80 μWh, this error is negligible.

An N-channel enhancement mode MOSFET is used as a switch to connect the voltage divider to the supercapacitor when an energy level measurement is required. The Nexperia BSH105 is chosen for its low threshold voltage of 0.57 V, its low leakage current of 50 nA when zero volt is applied to the gate, and its low on-resistance of 1.18 Ω at a gate to source voltage $V_{GS} = 1.5\,V$ [37]. The switch is controlled by the MCU that asserts an IO pin when a measurement is required, shown as MCU_on/off in Figure 5.2. However, the maximum output voltage of such a pin is 1.8 V. Since the maximum source voltage V_S of the MOSFET is 1.7 V, a V_{GS} of only 0.1 V can be achieved, while to forward bias the MOSFET a V_{GS} of at least 0.57 V is required. Therefore, a voltage amplifier is used to increase the gate voltage applied to the MOSFET.

When no measurement is required the control signal of the MCU should be low. The datasheet of the MCU shows that a maximum of 0.45 V can be present due to noise at the output of the IO pin when it is pulled low. To prevent amplifying this noise, a diode and resistor are used in front of the amplifier. The diode used is the 1SS307E from Toshiba, as it is able to block the noise voltage with a current in the nA range [38]. It is important that this current is low, since this determines the static power drawn from the MCU. Notice that in order to get the threshold voltage across the diode, this minimal current must flow. The opamp has an almost infinite input resistance, thus the minimal current is not reached with solely the diode. To solve this problem a resistance of 100 $k\Omega$ is connected between the positive terminal of the opamp and ground and creates a diode current flow of

$$I_{R5} = \frac{V_{MCU\_on/off,max} - V_{f,D1}}{R5} = \frac{1.8 - 0.61}{100 \cdot 10^3} = 11.90\,\mu A$$

where $V_{MCU\_on/off,max}$ is the maximum output of the IO pin of the MCU, and $V_{f,D1}$ is the forward voltage drop of the diode. This current results to be sufficient for the intended operation of the diode.

The TLV8801 ultra low power operational amplifier from Texas Instruments is used as amplifier. It can operate at a single supply up to 5.5 V, and has a quiescent current I_Q of 450 nA [39]. As the source voltage V_S of the MOSFET can have a maximum voltage of 1.7 V, a gate voltage of at least $V_G = 0.57 + 1.7 = 2.27V$ is required for the MOSFET to be forward biased. The datasheet of the MOSFET shows that it is maximally forward biased for a V_{GS} of 1.5 V, and therefore the output of the amplifier should be $V_o = 1.5 + 1.7 = 3.2V$. The output voltage for the amplifier in Figure 5.2 is given as

$$V_o = \frac{R3 + R4}{R4} V_{in}$$

where $V_{MCU\_on/off}$ is the voltage of the MCU_on/off pin of the MCU, and is connected to anode of the diode. A factor of

$$\frac{R3 + R4}{R4} = \frac{V_o}{V_{MCU\_on/off,max} - V_{f,D1}} = \frac{3.2}{1.19}$$

is required to obtain an output V_o of 3.2 V. This implies that

$$R3 \approx 1.69 \cdot R4$$

To limit the current in the feedback network, the values 845 $k\Omega$ and 500 $k\Omega$ are used for $R3$ and $R4$ respectively, which results in a maximum current of

$$I_{fb,max} = \frac{V_{o,max}}{R3 + R4} \approx 2.38\,\mu A$$

which is 16.8 times smaller than the maximum current flowing through the voltage divider. As a consequence, the power consumption of the opamp low and equal to

$$P_{opamp} = (I_Q + I_{fb,max}) V_{C,max} = 15.0\,\mu Wh$$

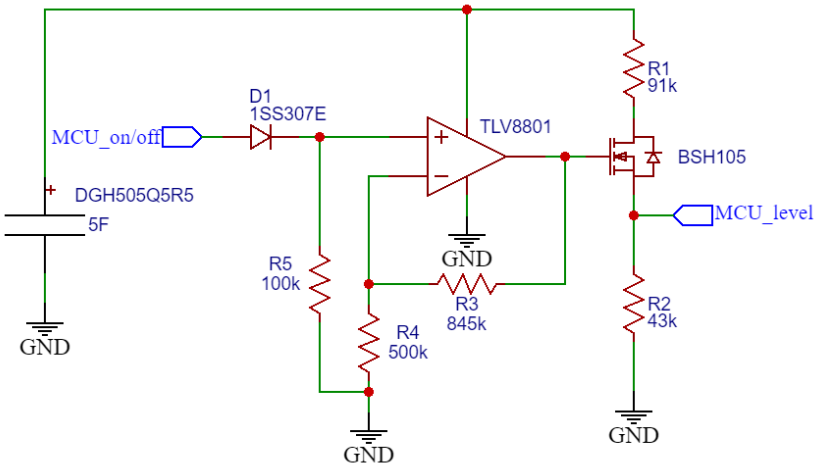

Figure 5.2: Schematic of the implementation of the supercapacitor energy monitoring system.

5.3.2 Verification of energy monitoring circuit

Now that design of the energy level monitoring circuit has been explained, the focus is set on the verification of the implementation. This verification is done with an Orcad-PSpice simulation, using the component libraries of the Nexperia BSH105, Toshiba 1SS307E and Texas Instruments TLV8801. These libraries help to create an application-specific and accurate simulation of the circuit. The full simulation setup and results are further discussed in Appendix E.3.

The result of the PSpice simulation is provided in Figure 5.3. This figure shows the simulated output signal of the energy monitoring circuit that is measured at the input of the ADC of the MCU. The output is plotted as a function of the supercapacitor voltage in the range of 2.2 V to 5.4 V, for the cases that the MCU_on/off is set low or high, 0.00 V and 1.80 V respectively. When MCU_on/off is set at 1.8 V, the graph clearly shows the linear relationship between the supercapacitor voltage and the V_{MCU_level} as intended in Equation 5.3.1. If V_C = 2.2 V this results in a simulated V_{MCU_level} = 0.71 V, and if V_C = 5.3 V this results in a simulated V_{MCU_level} = 1.70 V, both fully satisfy the intended relation. In contrast, when MCU_on/off is set at 0.0 V, the graph shows no relationship between the supercapacitor voltage and the V_{MCU_level}. This is because the MOSFET is shut off, causing almost no current to flow through the resistor divider, and therefore power is saved. The potential measured at the MCU_level pin is constant at 33 mV.

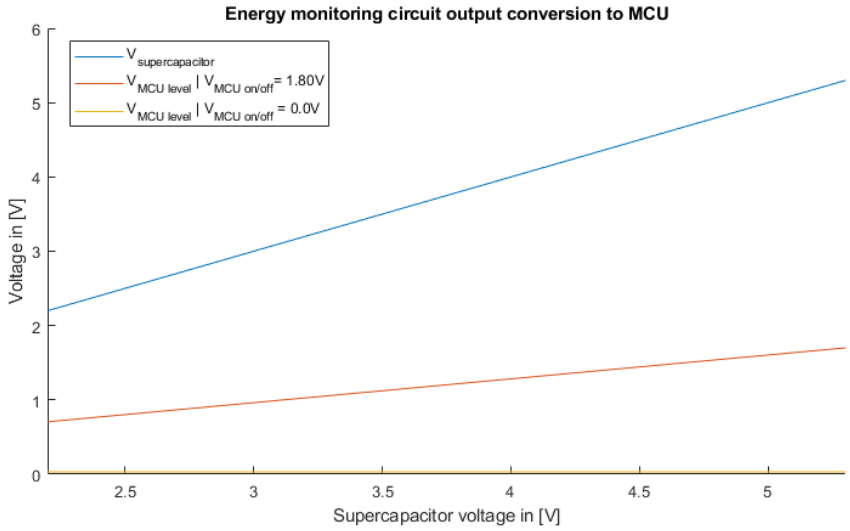

Figure 5.3: Plot of the simulated output MCU_level of the energy monitoring circuit as a function of the supercapacitor voltage when MCU_on/off is set low (0.00 V) and high (1.80 V).

From the extended simulation provided in Appendix E.3 can be concluded that the whole design performs as intended. The quiescent current, when MCU_on/off is set at 0.0 V, is maximum 0.51 μA for the opamp and 0.76 μA for the MOSFET. Similarly, the operation current when MCU_on/off is set at 1.8 V is maximum 2.88 μA for the opamp, 11.87 μA for the MCU, and 39.47 μA for the MOSFET. These maximum operation and quiescent current do occur when the supercapacitor is fully charged and are approximately similar to the theoretical values calculated in Section 5.3.1.

To make an estimation of the energy consumption of the energy monitoring circuit, an estimate of the measurement time is needed. Because of the capacitive behaviour of the gate of the MOSFET and the terminals of the opamp, the current flow through the MOSFET is not instantaneous. To determine the required time to complete a measurement, a transient simulation is done for the monitoring circuit. The result of the simulation is provided in Figure 5.4. This figure shows the input voltage $V_{MCU\_on/off}$, which ramps from 0.0 V to 1.8 V at 1 ms, and the corresponding output voltage V_{MCU_level} as a function of time.

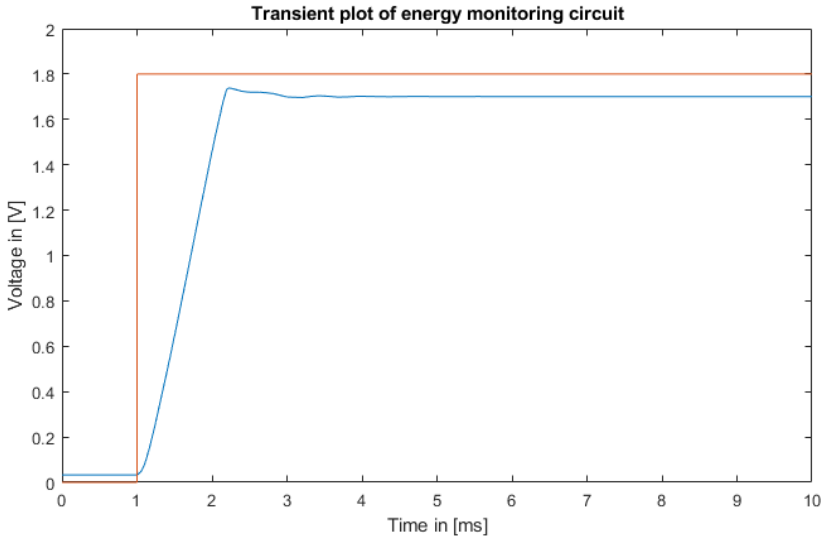

Figure 5.4: Time domain plot of the output of the energy monitoring circuit when the MCU_on/off is set high, 1.8 V, at 1 ms and the supercapacitor voltage is fixed at 5.3 V.

From the figure can be concluded that the transient time required for the V_{MCU_level} to stabilise is 3.0 ms. This simulation was done using the worst-case supercapacitor voltage of 5.3 V, decreasing this voltage causes the delay time to drop below 3.0 ms. After the measurement is done, the V_{MCU_level} must also stabilise back to 0.0 V, which takes again 3.0 ms, therefore the total estimated time period needed for the measurement is approximately 8.0 ms, in which 6.0 ms are needed for the setup and shutdown of the system and 2.0 ms are available for the ADC to measure the voltage. During these 8.0 ms, the maximum operation current drawn from the supercapacitor is 42.35 μA, and the maximum current drawn from the MCU_on/off is 11.87 μA. When the energy level is not measured the quiescent current drawn from the supercapacitor is 1.27 μA. Thus, the total daily energy consumption is estimated at a worst-case of

$$E = active\_power \cdot time\_measurement \cdot amount\_of\_measurements + quiescent\_power \cdot 24hours$$
$$= (42.35\mu A \cdot 5.3V + 11.87\mu A \cdot 1.8V) \cdot \frac{8.0 \cdot 10^{-3}}{3600} \cdot (24h \cdot 12measurements/h) + (1.27\mu A \cdot 5.3V) \cdot 24h = 0.162mWh$$

So the designed energy monitoring circuit as given in Figure 5.2 performs as intended and has a worst-case daily energy consumption of 0.162 mWh. Note that this estimate is a worst-case estimation, in which the highest frequency of energy level monitoring is used and the supercapacitor voltage is at its highest voltage of 5.3 V.

Chapter 6

Complete system implementation

The previous chapters each elaborated on the design and implementation of parts of the energy harvesting and control module. Now that these individual components are known, this chapter further elaborates on the implementation of the complete system. Also, when implemented, the energy control module is simulated to verify its operation. Finally, this chapter concludes the full system verification in the form of a reliability analysis based on the past 10 years of temperature and solar irradiance data.

6.1 Energy control module implementation

As was mentioned in Chapter 4, the energy harvesting module is implemented using the SM500K12L solar cell as the main energy source. This solar cell is then connected to the SPV1050, which serves as the main control unit. This control unit takes care of the maximisation of the energy harvesting efficiency of the solar cell, provides charging control of the supercapacitor, gives two stable outputs, and has a low quiescent and operation power consumption. The SPV1050 is connected to the solar cell, supercapacitor, microcontroller and wireless communication module.

6.1.1 Design of energy control module

Figure 6.1 shows the implementation of the SPV1050, where it is connected to the remaining components via the indicated arrows. For proper implementation of the SPV1050, the correct component values must be chosen for the resistors $R1 - R6$, capacitors $C1 - C5$, and inductor $L1$.

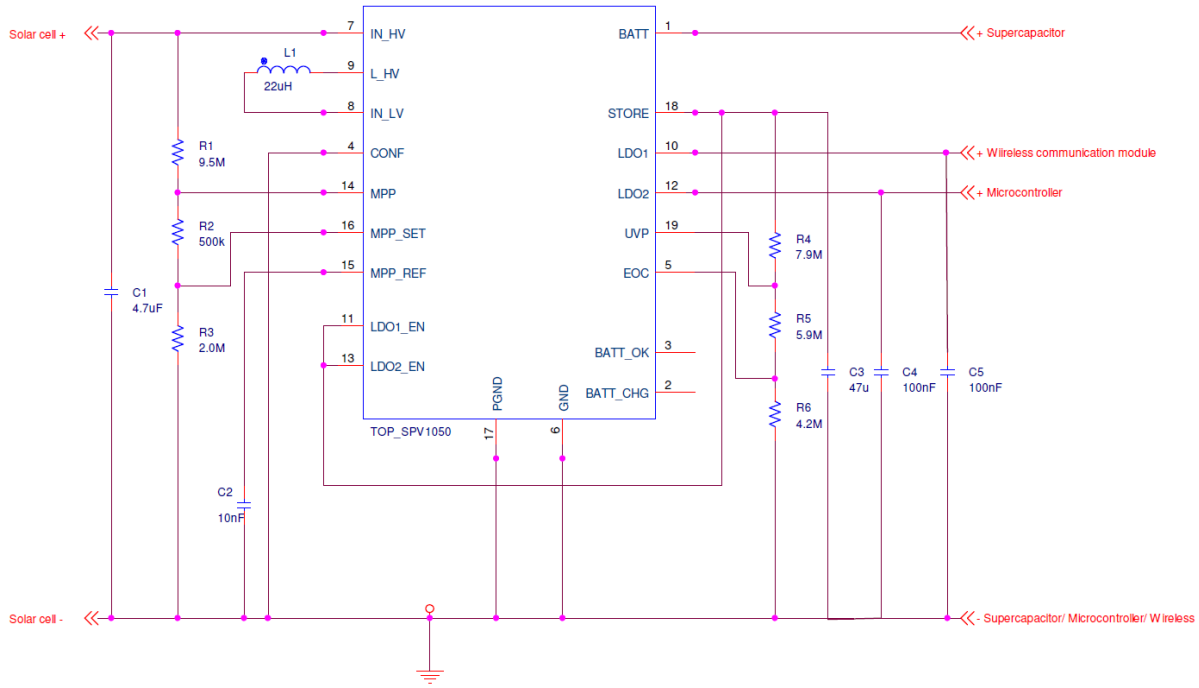

Figure 6.1: This figure shows the implementation of the SPV1050 as the energy control module when it is connected to the solar cell, supercapacitor, microcontroller and wireless communication module.

First, the values of the resistors $R1$, $R2$ and $R3$ are chosen. These values are determined by using Equations 6.1, 6.2 and 6.3 which are provided in the datasheet of the SPV1050 [32].

$$10\ M\Omega \leq R1 + R2 + R3 \leq 20\ M\Omega \tag{6.1}$$

$$R2 + R3 \leq (R1 + R2 + R3) \cdot \frac{V_{UVP(min)}}{V_{OC}} \tag{6.2}$$

$$MPP_{Ratio} = \frac{R3}{R2 + R3} \tag{6.3}$$

These resistances are used by the SPV1050 to fix the MPP voltage of the solar cell. As was mentioned in Section 4.2, the voltage at which maximum power is delivered by the solar cell is variable between 6.4 V and 7.0 V, depending on the irradiance. The MPP voltage can therefore be defined as a ratio of the open circuit voltage, MPP_{Ratio}, which according to the datasheet is 6.7/8.29 = 0.81. The MPPT module of the SPV1050 finds the MPP voltage by sampling the open circuit voltage of the solar cell and multiplying it by the MPP_{Ratio}. The SPV1050 puts this MPP voltage across the terminals of the solar cell. Initially, the resistors sum of $R1$, $R2$ and $R3$ was set at 18 $M\Omega$ to comply with Equation 6.1. However, during simulation was found that these values were too high as the voltages at MPP and MPP_SET did not fully stabilise during an open circuit sampling, causing them to be sampled too low which resulted in a too low MPP voltage. So the sum of $R1$, $R2$ and $R3$ was set at 12 $M\Omega$, in which $R1 = 9.5\ M\Omega$, $R2 = 500\ k\Omega$ and $R3 = 2\ M\Omega$, fully satisfying Equations 6.1, 6.2 and 6.3. With these values the voltages at MPP and MPP_SET stabilised, and the MPP_{Ratio} is set at 80% of the open circuit voltage.

Next, the values of capacitors $C1$ and $C2$ are chosen. Capacitor $C2$ is set at 10 nF as indicated in the datasheet [32]. Capacitor $C1$ is chosen such that it meets the inequality set by Equation 6.4, in which $T1$ is the time constant of $C1$ and the equivalent resistance of the solar cell R_{EQ}, which is given by Equation 6.5.

$$C_1 \leq \frac{T_1}{R_{EQ}} \tag{6.4}$$

$$R_{EQ} = \frac{V_{OC} - V_{MPP}}{I_{MPP}} \tag{6.5}$$

This time constant needs to be less than one fifth of the 400 ms sampling period of the SPV1050. From this follows that $C1$ must be lower than 996 μF. $C1$ is set at $4.7\mu F$ as advised in the datasheet, which meets the inequality.

Similar to the way resistors $R1$-$R3$ control the MPPT module, resistors $R4$-$R6$ are used to control the charging of the supercapacitor. The SPV1050 has an undervoltage protection (UVP), V_{UVP}, that limits the usage of the supercapacitor when its terminal voltage drops below this level. The V_{UVP} is set at its lowest possible value of 2.2 V, since there is no lower limit imposed by the supercapacitor, so maximum storage range can be used. Similarly, the SPV1050 also has an end-of-charge voltage V_{EOC} which is set at the highest value of 5.3 V. Both V_{UVP} and V_{EOC} are obtained by again using a voltage divider. To find the values of $R4$-$R6$ at first the sum of the three resistors is set at 18 $M\Omega$ such that it meets the requirement given in Equation 6.6 [32].

$$10\ M\Omega \leq R4 + R5 + R6 \leq 20\ M\Omega \tag{6.6}$$

Next, by using Equations 6.7 and 6.8 provided in the datasheet [32], the resistor values are calculated to be $R4 = 7.9\ M\Omega$, $R5 = 5.9\ M\Omega$ and $R6 = 4.2\ M\Omega$, to meet the desired values of V_{UVP} and V_{EOC}.

$$(R5 + R6) = (R4 + R5 + R6) \cdot \frac{1.23}{V_{UVP}} \tag{6.7}$$

$$R6 = (R4 + R5 + R6) \cdot \frac{1.23}{V_{EOC}} \tag{6.8}$$

Finally, capacitances $C3$, $C4$ and $C5$ are chosen to be 47 μF, 100 nF and 100 nF respectively, as is advised in the datasheet of the SPV1050 buck-boost implementation [40].

6.1.2 Verification of energy control module

The implementation of the SPV1050, shown in Figure 6.1, is simulated in Orcad-PSpice to verify the design using the component library provided by STmicroelectronincs [32]. The full simulation setup and plots of the results are shown in Appendix E.4. The simulation is done for two cases. The first one is for the case where the supercapacitor is initially completely discharged, so it has a voltage of 0 V, and the SPV1050 starts operating in startup mode. The second one is for the case the supercapacitor has a voltage of 4 V, and the SPV1050 starts operating in normal operation mode. In both cases, the simulation shows consistent results.

The open-circuit voltage is measured to be 8.29 V and the MPP voltage is kept at 6.57 V, which gives a MPP_{Ratio} of 6.57/8.29 = 0.793. The accuracy of the MPP voltage applied to the solar cell by the SPV1050 is at least 95% [32], thus the minimum allowable MPP_{Ratio} is $0.95 \cdot 0.8 = 0.760$. Therefore, the MPP_{Ratio} is correct. Further, capacitor C_1 is chosen correctly as the measured V_{oc} during sampling equals 8.29 V, which is the open-circuit voltage of the solar cell. This indicates that the time constant $T1$ is small enough to obtain correct MPPT measurements. The measured end of charge voltage V_{EOC} equals 5.26 V. The datasheet shows that it has an accuracy of -1% due to hysteresis, and with the designed 5.27 V this results in a lower limit $V_{EOC,min}$ of $0.99 \cdot 5.27 = 5.22V$. Therefore it can be concluded that V_{EOC} value is correct. Further, the measured under-voltage protection V_{UVP} equals 2.20 V, which is precisely the desired value. From these simulation results and the results provided in Appendix E.4 can be concluded that the SPV1050 as the main control unit of the energy harvesting module is implemented correctly.

6.2 Complete system reliability analysis

With the implementation of the SPV1050 as discussed in the previous section, the full energy harvesting and control system has been implemented. In this section, a complete system reliability analysis is done to verify the long term operation of the implemented energy system. The simulation is created based on the top-level power breakdown of the system that is provided in Appendix A.3.

The complete system reliability simulation is an evolved version of the simulation done in Section 4.1.1, were the daily energy harvested by a solar cell was calculated based on the solar irradiance data. The complete system reliability analysis calculates the amount of energy stored in the supercapacitor as a function of time, given the incident irradiance, temperature, and power consumption of the system. The simulation makes use of hourly temperature and solar irradiance data from February till June in the years 2009-2019 at station 269 Lelystad [26]. Furthermore, it is based on several assumptions, including assumptions A1 and A2 as explained in Section 4.1.1, as well as the following assumptions:

A4. The incident irradiance and temperature are assumed to vary linearly between the hourly data points.
A5. The conversion efficiency of the SPV1050 is estimated to be constant at 84% and is independent of the solar irradiance or the supercapacitor voltage level.
A6. The sensor node operates in normal operation mode, as explained in Appendix A.2, where each energy level measurement takes 8 ms, as explained in Section 5.3.2. This mode is used unless the supercapacitor voltage drops below 3.3 V, then no transmissions are done until the supercapacitor voltage rises above 3.3 V again.

The two LDOs of the SPV1050 provide a constant 1.8 V and 3.3 V at the output. An LDO generates an output voltage by using a controlled variable resistor and so internally dissipates energy. The efficiency of conversion is given by Equation 6.9. Especially for the 1.8 V LDO this efficiency can be quite low, down to 34%. To solve this problem several solutions are provided in Section 7.2

$$\eta = \frac{V_{LDO}}{V_{Supercapacitor}} \tag{6.9}$$

The result of the reliability simulation is given in Figure 6.2a. This figure shows the energy level of the supercapacitor as a function of time for week 6 in 2009. The simulation is made using the weather data of that week, which is provided in Figure 6.2b. At midnight, time = 0 h, the capacitor is for 80% charged and starts losing energy rapidly due to the leakage of the supercapacitor and the high measurement frequency, which is needed because of the low temperature. At time = 7 h the incoming solar irradiance starts to increase

and the supercapacitor quickly charges up to its maximum of 11.94 mWh. This continues up to time = 16 h, then the energy consumption of the sensor node becomes higher than the energy harvested by the solar cell, and the energy stored in the supercapacitor starts to decrease. This cycle continues every day. The figure also indicates that the effect of a low-temperature day is significant on the energy consumption. When the temperature gets close to the critical temperature of 0 °C the sensor node increases the measurement frequency, resulting in a larger energy consumption. In this week, the difference in lowest energy storage level between a cold day like day 2 and relatively warm day like day 6 is 2.81 mWh. The same analysis for the supercapacitor being initially 0% charged is provided in Appendix E.5.

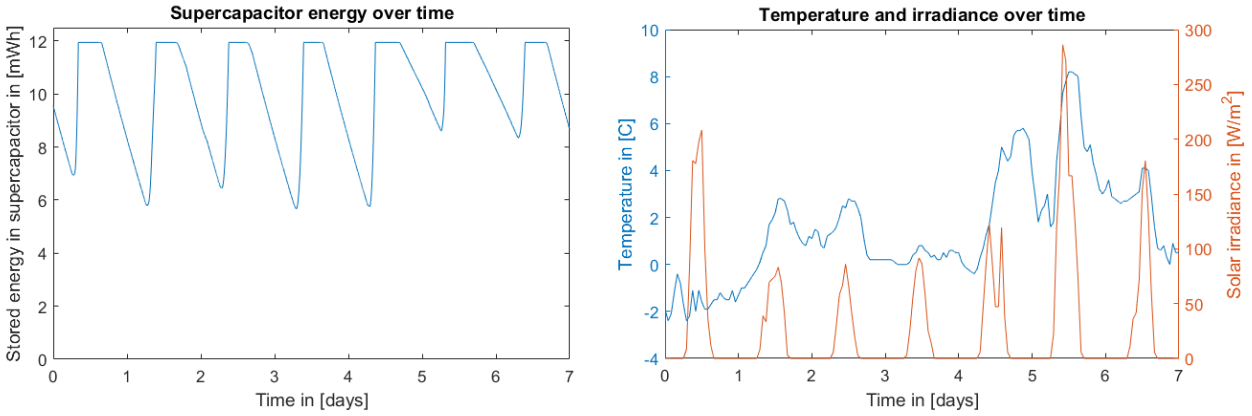

(a) This figure shows the energy level of the supercapacitor as a function of time. *(b) This figure shows the temperature and solar irradiance of week 6 in 2009.*

Figure 6.2: The amount of energy stored in the supercapacitor, the temperature, and solar irradiance as a function of time using the designed energy harvesting and control module. The graphs are based on week 6 in 2009, and uses an initially 80% charged supercapacitor.

In addition to executing the complete system reliability analysis for a weekly period, the simulation is also done for the months February till June in the years 2009-2019. The result of this simulation is given in Figure 6.3. This figure shows a histogram indicating the minimal energy level in the supercapacitor that was reached during a day. This minimum energy level usually occurs just before sunrise and is on average 9.07 mWh. The lowest minimal energy of the supercapacitor that occurred in these 10 years of spring data is 5.45 mWh. This worst case is further evaluated in Appendix E.5.

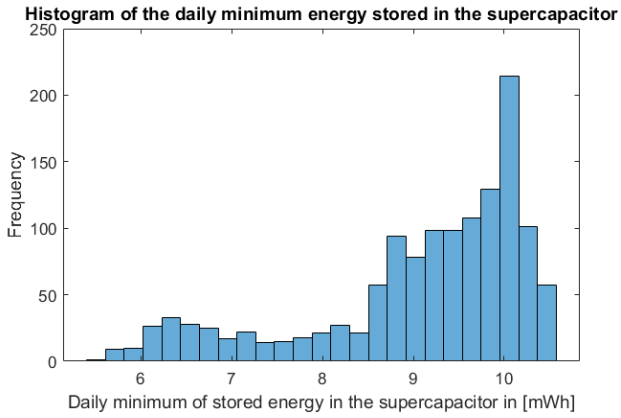

Figure 6.3: This figure shows a histogram of the daily minimum energy level of the supercapacitor. The simulation is based on February till June for 2009 up to 2019.

So from the complete system reliability simulation can be concluded that the implemented energy harvesting and control module performs as intended. According to the past 10 years of spring data, no loss of operation would occur, even if days occur where almost no ambient solar energy is present and temperatures are below the critical temperature. The energy harvesting and storage are therefore large enough to sustain all energy consumption of the sensor while it is performing its intended operation.

Chapter 7

Conclusion and Future Work

7.1 Conclusion

The Autonomous Temperature Sensor for Smart Agriculture project focuses on the acquisition of the 3D temperature profile of a fruit orchard. The main goal of the energy harvesting and control group is to design and implement an energy module that can sustain all energy needs of the sensor nodes. Since the sensor nodes must be able to locally harvest their consumed energy, an energy module is implemented that harvests the energy from an ambient energy source, controls the flow of power, stores the energy, and provides the energy level of the storage to the MCU. This implementation results in a durable and cost effective solution that guarantees a high continuity of operation.

The first design step concludes the choice of ambient energy source. From the four possible ambient energy sources, solar energy was found the most suitable. Simulations of the power density of RF energy showed that it is not able to sustain the minimal power requirements of the sensor nodes. For wind energy, the harvesting techniques were found not reliable enough to guarantee an operation time of 20 years. Due to the lack of significant temperature differences, thermal energy is not considered applicable. On the contrary, simulations showed that abundant energy can be harvested using solar energy. The solar cell used is the SM500K12L from IXYS. The second design step concludes the control module used for the solar cell. The choice between a diode implementation and a complex MPPT module is made. The MPPT module is chosen over the diode implementation, because the charging efficiency as well as the harvested power cannot be controlled using the diode implementation, and are both minimal when the supercapacitor is depleted. Moreover, the MPPT module that is used, the SPV1050, has two LDOs at the correct output voltages to supply power to the wireless communication module, the MCU and temperature sensors. The third design step was to consider the energy storage module. Several implementations of energy storage were taken into account from which the EDLC was concluded the best. Although the supercapacitor has a high leakage, it excels in long term reliability, thereby is better than the alternatives. The chosen storage module is the DGH505Q5R5, a 5 F EDLC with a maximum leakage current of 30 μA. Directly connected to the supercapacitor is the energy level monitoring, a circuit that uses a smart implementation of a voltage divider to guarantee high accuracy while sustaining low static energy consumption. The MCU can fully control the monitoring circuit, and measures the energy level using a 12bit ADC.

The implemented energy harvesting and control module was simulated to find that it sustains all power and system demands, thereby complying with the requirements. Regarding the simulations results, each justified the design choices and therefore conclude a correct and applicable implementation of the module.

7.2 Future work

The SPV1050 distributes power to the sensor node using two LDOs. But as was concluded in Section 6.2, the efficiency of these LDOs is quite low. For the 1.8 V and 3.3 V LDO, a worst case conversion efficiency of 34% and 63% can be achieved respectively. This significantly increases the energy consumption of the SPV1050. Despite the fact that this did not result in a discontinuity of power supply, improvements can be made on the output characteristic of the module. Two design changes are proposed that may improve the efficiency of the energy control module, as well as the voltage range of the supercapacitor that can be used.

- Using the current design as a starting point, it is possible to connect two switched-mode DC-DC converters to the $STORE$ output pin of the SPV1050 to power the other modules, instead of using the LDOs. The efficiencies of these converters usually range up to 93%. This conversion efficiency is

much higher than the one obtained when using the built-in LDO regulators and is independent of the supercapacitor voltage. Most of the modules also have an on/off pin such that the converter can be switched off when no power is needed. This can be the case for the wireless communication unit, but more research and redesign must be conducted to verify if the module can be switched off to save quiescent power. It is proposed to use the Ablic S-85S0A DC-DC step down switching regulator, which has a conversion efficiency of 90.5% and the option to be shut off. It has a quiescent current of 260 nA during operation and a quiescent current of 1 nA in shut off mode. This regulator can be used for both the microcontroller and wireless communication module by choosing the S-85S0AB18-I6T1U version for the 1.8 V and the S-85S0AB33-I6T1U version for the 3.3 V. An alternative is to use a buck-boost converter as the 3.3 V DC-DC converter. This increases the usable energy stored in the supercapacitor by 35%, which may result in the possibility to use a smaller supercapacitor. It is proposed to use the LTC3130 from Linear Technologies, as it has an efficiency of 95% and a quiescent current of 1.6 μA. This component should not be used for the 1.8 V. The S-85S0A is still a better choice, as it has a lower quiescent current. Moreover, the supercapacitor gets disconnected from the $STORE$ pin when it decreases to 2.2 V, so no extension of the usable energy stored can be obtained.

- When using a completely different approach, the Texas Instruments BQ25570 can be used as the main control module of the solar cell. Even-though, in Section 4.2, this component is not considered as the best implementation of the control module, it might be a good solution for further development. Due to some late occurring design-changes in the autonomous temperature sensor for smart agriculture project, it might be better to use the BQ25570. This module, according to its specifications, has an input conversion efficiency of up to 93%, a leakage current of 488 nA and an output efficiency of up to 93%. This high output efficiency results from a buck converter implementation that is used as the output rather than an inefficient LDO implementation. Also, to create the second output, an external DC-DC converter is required. From the mentioned specifications follows that the BQ25570 could be more efficient than the SPV1050. However, it should be noted that as a result of the low input voltage range a significant change in solar cell is needed. Also concluded from section 6.2, the EDLC is often fully charged which results in the open circuit voltage to be across the input of the control module. The open circuit voltage can, under some conditions, exceed the datasheet value. Proper care should be taken to not overload the input of the BQ25570, which is not a problem when using the SPV1050. Because of the current restrictions no physical measurements could be done, and in addition there was not enough time. Both restricted our ability to fully analyse and review the BQ25570 as a real design option.

In addition to these design changes, an important aspect for future work would be to verify the implementation of the energy harvesting and control module by physically measuring the implemented circuit. This could not be done because of the current restrictions. Besides, long term operational testing should be done to verify the continuity and justify the storage choices.

References

[1] Harold van der Meulen, "Fruitareaal en aantal bedrijven," *https://www.agrimatie.nl/SectorResultaat.aspx?subpubID=2232&sectorID=2237*, 2020.

[2] J. Rodrigo, "Spring frosts in deciduous fruit trees. Morphological damage and flower hardiness," *Scientia Horticulturae*, vol. 85, no. 3, pp. 155–173, 2000.

[3] A. A. Ghaemi, M. R. Rafiee, and A. R. Sepaskhah, "Tree-Temperature Monitoring for Frost Protection of Orchards in Semi-Arid Regions Using Sprinkler Irrigation," *Agricultural Sciences in China*, vol. 8, no. 1, pp. 98–107, 2009.

[4] A. C. Ribeiro, J. P. De Melo-Abreu, and R. L. Snyder, "Apple orchard frost protection with wind machine operation," *Agricultural and Forest Meteorology*, vol. 141, no. 2-4, pp. 71–81, 2006.

[5] M. Huiskes and M. Miao, "Autonomous Temperature Sensor for Smart Agriculture - Smart Measurement and Control," 2020.

[6] A. Bleeker and R. Wijnands, "Autonomous Temperature Sensor for Smart Agriculture - Wireless Communication," 2020.

[7] M. S. Mahmoud and A. A. H. Mohamad, "A Study of Efficient Power Consumption Wireless Communication Techniques/ Modules for Internet of Things (IoT) Applications," *Advances in Internet of Things*, vol. 06, no. 02, pp. 19–29, 2016.

[8] F. J. Pierce and T. V. Elliott, "Regional and on-farm wireless sensor networks for agricultural systems in Eastern Washington," *Computers and Electronics in Agriculture*, vol. 61, no. 1, pp. 32–43, 2008.

[9] G. Sushanth and S. Sujatha, "IOT Based Smart Agriculture System," *2018 International Conference on Wireless Communications, Signal Processing and Networking, WiSPNET 2018*, pp. 1–4, 2018.

[10] S. Kim, R. Vyas, J. Bito, K. Niotaki, A. Collado, A. Georgiadis, and M. M. Tentzeris, "Ambient RF energy-harvesting technologies for self-sustainable standalone wireless sensor platforms," *Proceedings of the IEEE*, vol. 102, no. 11, pp. 1649–1666, 2014.

[11] W. Bacharowski, "Energy scavenging for remote sensors," *Electronic Design*, vol. 53, no. 28, 2005.

[12] M. Penella and M. Gasulla, "A Review of Commercial Energy Harvesters for Autonomous Sensors," pp. 1–5, 2007.

[13] S. Fajardo, García-Galvan, F. R., V. Barranco, J. C. Galvan, and S. F. Batlle, "Thermoelectric Energy Harvesting: Basic Principles and Applications," *Intech*, vol. i, no. tourism, p. 13, 2016.

[14] B. V. Novem, "Optimale positionering van PV arrays Samenvatting," 2002.

[15] Team ProductLine, "Solar panel cost: Price range of different types of solar panels and how much govt. subsidy can you avail for installing one," 2019.

[16] F. K. Shaikh and S. Zeadally, "Energy harvesting in wireless sensor networks: A comprehensive review," *Renewable and Sustainable Energy Reviews*, vol. 55, pp. 1041–1054, 2016.

[17] D. Jordan, T. Silverman, J. Wohlgemtuh, S. Kurtz, and K. VanSant, "Photovoltaic failure and degradation modes," *Ieee Trans Fuzzy Syst*, vol. 20, no. 6, pp. 1114–1129, 2012.

[18] E. Echavarria, B. Hahn, G. J. Van Bussel, and T. Tomiyama, "Reliability of wind turbine technology through time," *Journal of Solar Energy Engineering, Transactions of the ASME*, vol. 130, no. 3, pp. 0310051–0310058, 2008.

[19] H. A. Sodano, D. J. Inman, and G. Park, "Generation and storage of electricity from power harvesting devices," *Journal of Intelligent Material Systems and Structures*, vol. 16, no. 1, pp. 67–75, 2005.

[20] KNMI, "Gemiddelde windsnelheid Nederland 1981-2010," *http://www.klimaatatlas.nl/klimaatatlas.php?wel=wind&ws=kaart&wom=Gemiddelde%20windsnelheid*.

[21] A. N. Parks, A. P. Sample, Y. Zhao, and J. R. Smith, "A wireless sensing platform utilizing ambient RF energy," *BioWireleSS 2013 - Proceedings: 2013 IEEE Topical Conference on Biomedical Wireless Technologies, Networks, and Sensing Systems - 2013 IEEE Radio and Wireless Week, RWW 2013*, vol. 98195, pp. 154–156, 2013.

[22] Rijksoverheid, "Antenna register," *Accessed on: May 07, 2020. [Online]. Available: https://antenneregister.nl/Html5Viewer/Index.html?viewer=Antenneregister_extern*.

[23] Rijksoverheid, "Nationaal frequentiebeleid," *November 25, 2014, Accessed on: May 7, 2020. [Online]. Available: https://zoek.officielebekendmakingen.nl/stcrt-2014-33116.html*, 2014.

[24] Rijksoverheid, "Mobiele telecommunicatie (2G, 3G, 4G en 5G)," *March 19, 2018, Accessed on: May 8, 2020. [Online]. Available: antennebureau.nl/antennes-en-teachniek/soorten-antennes/antenne-voorbeeld*.

[25] CBS, "Landbouw; gewassen, dieren en grondgebruik naar regio," *https://www.cbs.nl/nl-nl/cijfers/detail/80780NED?d*, 2020.

[26] KNMI, "Uurgegevens van het weer in Nederland," *Accessed on: May 20, 2020. [Online]. Available: https://projects.knmi.nl/klimatologie/uurgegevens/selectie.cgi*.

[27] M. Chegaar, A. Hamzaoui, A. Namoda, P. Petit, M. Aillerie, and A. Herguth, "Effect of illumination intensity on solar cells parameters," *Energy Procedia*, vol. 36, pp. 722–729, 2013.

[28] I. Edinbarough, "Experimental study on the optimum harvesting of sunlight for an efficient solar energy system," *ASEE Annual Conference and Exposition, Conference Proceedings*, 2013.

[29] Z. Nagy, B. Svetozarevic, P. Jayathissa, M. Begle, J. Hofer, G. Lydon, A. Willmann, and A. Schlueter, "The Adaptive Solar Facade: From concept to prototypes," *Frontiers of Architectural Research*, vol. 5, no. 2, pp. 143–156, 2016.

[30] D. Brunelli, L. Benini, C. Moser, and L. Thiele, "An efficient solar energy harvester for wireless sensor nodes," *Proceedings -Design, Automation and Test in Europe, DATE*, pp. 104–109, 2008.

[31] L. M. Fraas and L. D. Partain, *Solar Cells and Their Applications*. John Wiley & Sons, Incorporated, 2010.

[32] "Ultralow power energy harvester and battery charger," *STMicroelectronics. SPV1050 datasheet, May 2018.*

[33] Nexperia, "RB751 series Schottky barrier single diodes," *RB751 datasheet, May 2007*.

[34] I. Buchmann, "Secondary Batteries.," *August 6, 2019, Accessed on: April 24, 2020. [Online]. Available: https://batteryuniversity.com/learn/article/secondary_batteries*.

[35] "VPC0820 _ 3.8V 30F," *VINATech. VEL08203R8306G datasheet.*

[36] L. Yang, S. Cheng, Y. Ding, X. Zhu, Z. L. Wang, and M. Liu, "Hierarchical network architectures of carbon fiber paper supported cobalt oxide nanonet for high-capacity pseudocapacitors," *Nano Letters*, vol. 12, no. 1, pp. 321–325, 2012.

[37] "N-channel enhancement mode BSH105 MOS transistor," *Nexperia. BSH105 datasheet. August 1998*.

[38] "Toshiba Switching Diodes 1SS307E," *Toshiba. 1SS307E datasheet. November 2018*.

[39] "TLV8801/TLV8802 320 nA Nanopower Operational Amplifiers for Cost-Optimized Systems," *Texas Instruments. TLV8801 datasheet. November 2016*.

[40] D. Ragonese, "Evaluation board for SPV1050 ULP harvester (buck-boost architecture)," no. June 2016, p. 19.

[41] M. Murray, "Critical Temperatures for Frost Damage on Fruit Trees," *Utah State University*, 2020.

[42] M. V. D. Sluys, "Instraling door de zon in Nederland Voor daken op het oosten , westen of noorden zijn horizontale," vol. 2, pp. 1–5, 2016.

[43] X. Lu, P. Wang, D. Niyato, D. I. Kim, and Z. Han, "Wireless networks with rf energy harvesting: A contemporary survey," *IEEE Communications Surveys and Tutorials*, vol. 17, no. 2, pp. 757–789, 2015.

[44] D. Bouchouicha, F. Dupont, M. Latrach, and L. Ventura, "Ambient RF energy harvesting," *Renewable Energy and Power Quality Journal*, vol. 1, no. 8, pp. 1309–1313, 2010.

[45] H. J. Visser, A. C. Reniers, and J. A. Theeuwes, "Ambient RF energy scavenging: GSM and WLAN power density measurements," *Proceedings of the 38th European Microwave Conference, EuMC 2008*, no. October, pp. 721–724, 2008.

[46] R. J. Vyas, B. B. Cook, Y. Kawahara, and M. M. Tentzeris, "E-WEHP: A batteryless embedded sensor-platform wirelessly powered from ambient digital-TV signals," *IEEE Transactions on Microwave Theory and Techniques*, vol. 61, no. 6, pp. 2491–2505, 2013.

[47] A. M. Makarieva, V. G. Gorshkov, D. Sheil, A. D. Nobre, and B.-L. Li, "Where do winds come from? A new theory on how water vapor condensation influences atmospheric pressure and dynamics," *Atmospheric Chemistry and Physics*, vol. 13, pp. 1039–1056, 1 2013.

[48] J. G. Slootweg, S. W. H. de Haan, H. Polinder, and W. L. Kling, "Wind Power and Voltage Control," in *Wind Power in Power Systems*, ch. 19, pp. 411–432, John Wiley & Sons, Ltd, 2005.

[49] D. Ramasur and G. P. Hancke, "A wind energy harvester for low power wireless sensor networks," *2012 IEEE I2MTC - International Instrumentation and Measurement Technology Conference, Proceedings*, pp. 2623–2627, 2012.

[50] G. Laštovička-Medin, "The WindBelt as a Low-Cost Energy Generator: Low Energy Consumption Sustainable Solutions within the Framework of Modelling Pedagogy," *International Journal of Contemporary ENERGY*, vol. 4, no. 1, pp. 26–39, 2018.

Appendix A

The top-level system

A.1 Top-level system implementation

Before the three subsystems are designed, the implementation of the entire system is considered. The goal of the implementation is such that it fits the requirements of the entire system and that each subsystem can comply with their own requirements. When all these requirements are met, aspects that have to be reduced are manufacturing cost, deployment cost and maintenance cost. Furthermore durability has to be taken into consideration. To prevent confusion, a single node is defined as a subsystem with one wireless communication module, one microcontroller and one energy harvesting module. The possible implementations of the system that were considered to fit into the requirements of the system are the following:

- **Tree multi node:** An implementation where each single node has one temperature sensor. As a result a tree contains 5 separate nodes all on one tree. These multiple nodes are placed at different heights in the tree. This is a multi node implementation in a tree.
- **Tree single node:** A system where each node consists of a single MCU, wireless communication module and energy harvester, while multiple temperature sensors are connected to this single MCU. All sensors are placed in a tree at different heights.
- **Pole multi node:** A system where each node contains a single temperature sensor. Multiple nodes are placed on different heights on a pole.
- **Pole single node:** A system where each node has multiple connected temperature sensors and each node is integrated on a pole with the sensors at different heights.

To come to a design decision each option is weighted in the sections below. Based on this weight and the importance of each aspect an end decision is made which implementation is ultimately chosen.

Power consumption

The main power consumer is the wireless communication module. In a single node implementation, four wireless communication modules and MCUs are spared and thus this implementation is more preferable over a multi node implementation. The power consumption does not differ between a pole or tree implementation.

Cost

By implementing a single node structure, four wireless communication modules, four microcontrollers and four energy harvesting modules are spared compared to a multi node structure. This gives a single node structure more advantages. The purchase of a pole gives a tree implementation preference compared to the pole implementation, although this can be offset by the lower installation cost.

Durability

Durability assesses the life time of the system. A pole implementation is considered more durable than a tree implementation, since it has a more robust structure than the more fragile branches of a tree. For the pole implementation, it is difficult to assess whether a multi node or a single node implementation is better. However, in a single node implementation, less components are used and thus the chance of component failure is lower. On the other hand, in a single node implementation, temperature sensors are connected by wire and it depends on the type of integration whether this can have a signification negative impact on the device its lifetime.

Deployment

The deployment of the system assesses how easily the system can be installed. A significant advantage of a pole implementation is that it can be prefabricated and quickly installed by only planting the pole. For the tree, on-site installation has to be performed which can be quite labor intensive, since sensors have to be installed on a certain height. Regarding a multi node or single node solution, the only main difference is the wiring which comes with a single node system. This is concerned to be more dramatical in a tree than on a pole, since wiring of prefabricated poles can be implemented more easily.

Placement consistency

The consistency of the system assesses how uniform the heights of the sensors are for each of the trees/poles. For an implementation with a pole the distance between sensors can easily be made very consistent, whereas for the implementation in a tree, heights can be slightly different due to the fact that trees have different shapes. For this factor it does not matter whether a single-node or multi-node implementation is chosen.

Efficiency

The efficiency of the system describes how efficient the system can harvest energy and transmit signals. For a pole implementation with the antenna on top, the transmitted signal likely comes across less obstacles. Also with the solar panel on top of a pole instead of on a tree, the panel will receive a lot more solar energy due to the fact that there is less shadow from the tree itself. The difference between a multi-node implementation and single-node implementation also implies a difference in signal transmission- and energy harvesting efficiency. In the multi-node case, the solar panels are positioned on different heights. The nodes that are positioned higher will likely receive more solar radiation than lower positioned nodes. Furthermore transmitted signal from the nodes that are positioned lower will likely come across more obstacles.

Flexibility

The flexibility of the system describes the ease of changing the amount of sensors at a location. For a multi node pole implementation, the amount of sensors is changed with more ease than for a single node implementation. This is because, for a single node implementation, a sensor should be added or removed from the MCU, while for a multi node implementation only a complete module should be placed or removed without the need of connecting or disconnecting wires. The same holds for a tree implementation.

Maintainability

An important measure for designing a system is minimising the cost of maintenance after the system has been designed to reduce further costs and time. To maintain the system where each node has a single sensor greatly increases the amount of hardware that can fail and needs to be maintained. The time it takes to replace a node can be neglected in the comparison between multi and single node as it will have much less influence on the total maintenance cost then the total amount of hardware failures. To compare the tree and pole solution it comes to the same comparison as with deployment namely disassembling the node and installing it again.

Expandability

By implementing a single-node structure, more nodes can be added before the communication system gets saturated. This because of the limitation in the amount of wireless communication nodes that can be used for a certain gateway. By implementing a multi-node structure, the maximum amount of nodes gets reached more easily, and so the size of the sensor network becomes more limited.

Table A.1: Decision matrix for a tree or pole and multi- or single node implementation

		Tree multi node		Tree single node		Pole multi node		Pole single node	
Criterion	**Weight**	**Score**	**Weighted**	**Score**	**Weighted**	**Score**	**Weighted**	**Score**	**Weighted**
Power consumption	5	3	15	10	50	3	15	10	50
Cost	7	6	42	10	70	5	35	9	63
Durability	9	4	36	3	27	9	81	8	72
Deployment	2	4	8	3	6	10	20	10	20
Placement consistency	2	6	12	6	12	10	20	10	20
Efficiency	5	1	5	5	25	3	15	10	50
Flexibility	3	8	24	2	6	8	24	2	6
Maintainablity	7	1	7	8	56	2	14	9	63
Expandability	2	2	4	10	20	2	4	10	20
			153		272		228		364

Final decision

From Table A.1, it clear that, with a score of 364, a single node pole implementation is the best option for this application. The sub-modules in this project are designed according to this specific implementation. Also, resulting from the restricted energy consumption of the microcontroller group, the pole is set to have a maximum length of 3.0 m. This decision is justified further in their thesis [5]

A.2 Measurement operation

In order to determine the total amount of energy that is used by the sensor node, the operation of the measurement system is of importance. As is mentioned in the thesis of the microcontroller group [5], the measurement system has multiple modes of operation. These different modes are activated based on the energy level in the storage unit and external instructions from the base station. The normal, non-energy saving, operation mode is presented in Figure A.1. This figure shows the operation mode that is most often used, in which at least every half hour a measurement is done and the result is transmitted to the base station. In the case that the measured temperature gets close to the critical temperature of the fruit, the time between measurements is linearly decreased until a minimal interval of 5-minutes is reached. But, because the wireless communication module has a specific timeslot of transmission, the sensor node can only send its data at the possible transmission timeslots, which are at 5, 10, 15, 20 or 30 minutes [6]. The time at which is transmitted is always rounded down to one of these timeslots.
For the energy requirements calculations used by the energy harvesting unit, the critical temperature is put at 0 °C. The reason being that the system should be used for all kinds of fruit and so the critical temperature must be set relatively high. According to Murray (2011), there is a 10% decrease in fruit harvest if the fruit trees are exposed to -2.2 °C temperature for 30 minutes [41]. Therefore, to be sure that none of the fruit flower buds can be destroyed, the worst case of 0 °C is chosen.

In Figure A.1 a measure of 8.3 degrees is used as a reference for the maximum hourly change in temperature. This measure was found by analysing the temperature data of the past 10 years, looking at the maximum hourly decrease in temperature that resulted in the newest temperature being below zero. The data was obtained in the time period from February 2009 till June 2019 [26].

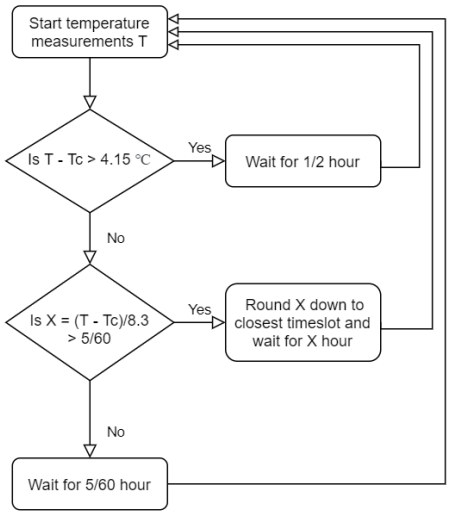

Figure A.1: Flowchart of the measurement system in case of normal operation, when no energy saving is active.

A.3 Top-level power breakdown

As is mentioned in Section 1.1, the autonomous temperature senor network consists of sensor nodes that are composted of a wireless communication module, microcontroller, multiple temperature sensors, and an energy harvesting module. Each of these components need energy to perform their operation. A full power breakdown is given in the table below, declaring the energy consumption of each of the individual components. For more information about the origin of the values for the wireless communication module see [6], and for the microcontroller and temperature sensor see [5].

Component	Value	Notes
Wireless communication module (RN2483)		
Quiescent power	5.28 μW	When in sleep mode
Energy consumption per transmission	13.80 μWh	Each transmission in worst case, scenario 4 SF10
Peak current	36.5 mA	During transmission
Operation voltage	3.3 V	
Microcontroller (STM32L151CBT6TR)		
Average power	2.406 μW	Sleep mode, active mode and I^2C combined
Peak current	7.8 mA	In case of full functional usage and I^2C in use
Operation voltage	1.8 V	
Temperature sensor (AS6212)		
Average power	0.18 μW	Sleep mode and active mode combined
Peak current	22.9 μA	During measurement
Operation voltage	1.8 V	
Energy controller (SPV1050)		
Static power when on	11.18 μW	With average storage voltage of 4.3 V
Static power when off	4.8 nW	With average storage voltage of 4.3 V
Conversion efficiency	84%	When operating in buck boost mode
Energy monitoring circuit		
Quiescent power	5.46 μW	When the voltage is not monitored
Operation power	203.47μW	During monitoring operation
Supercapacitor (DGH505Q5R5)		
Leakage current	30 μA	Worst case leakage

Appendix B

Background theory on types of ambient energy sources

This section provides background information on the ambient energy sources that can be used to power the wireless sensor nodes, together with the harvesters that are considered.

B.1 Solar energy

The first type of ambient energy source that can be used to power the sensors is solar energy. One of the biggest sources of energy on earth is the sun. The sun provides energy to the earth via electromagnetic radiation which can be harvested in various ways. In this section, the focus is put on the direct (primary) harvesting of electromagnetic solar radiation using PV cells. Later in this appendix, the secondary and tertiary solar energy sources are discussed in the form of wind energy and kinetic energy of the branches, respectively.

B.1.1 PV cell operation

The sun, because of its high temperature, radiates electromagnetic waves in all directions. Some of which penetrate through the atmosphere of the earth. These waves can also be seen as photons, the elementary particle representation of the wave. Each photon contains a discrete amount of energy depending on the frequency of the wave. This energy can be calculated by using the formula provided in Equation B.1. In this equation λ is the wavelength in meters, c is the speed of light ($2.998 * 10^8 m/s$) and h is the Planck constant.

$$E = \frac{h * c}{\lambda} \tag{B.1}$$

For some specific frequencies, the photon energy can be harvested and converted into electrical energy. This conversion is done by using photovoltaic cells. A photovoltaic cell or PV cell is a device that can convert the incoming electromagnetic radiation into electrical energy. This effect, also known as the photovoltaic effect, operates on specific light frequencies depending on the material properties of the PV structure. The PV cell consists of 2 types of semiconductor material, n-type and p-type, which are doped with donor and acceptor impurities respectively. When the photons that are incident upon a PV cell have a high enough photon energy, this energy can be absorbed by the semiconductor and as a result, a small excess charge is created on the terminals. If the PV cell is now connected to a load, the charge will flow and power is delivered to that load.

To deliver maximum power, the I-V characteristic of the PV cell is used. The formula for a general PV cell is provided in Equation B.2. In this equation V_{pv} and I_{pv} are the voltage across and current through the PV cell respectively, I_{sat} is the reverse saturation current of the pn junction and I_l is the light generated current [30]. From this equation, the maximum power can be determined using numerical approximation techniques and can be implemented using maximum power point tracking (MPPT) hardware.

$$I_{pv} = I_l - I_{sat}(e^{\frac{q}{A*k*T}(V_{pv}+I_{pv}*R_s)} - 1) \tag{B.2}$$

B.1.2 PV cell placement

To obtain the most amount of energy from a solar cell, the orientation with respect to the sun is of great importance. The PV cell should be oriented such that most of the incoming radiation incidents tangentially upon the surface. In the Netherlands the optimal placement of a solar cell is obtained at an elevation angle of 38°, the angle with respect to the horizon, and facing to the south at an azimuth angle of 182°. This placements is around 19% more efficient than a placement at an elevation angle of 0° [42]. In order to quantify the amount of incoming radiation, often solar time is used. The solar time is measured as the amount of hours of full solar power (1000 W/m^2 incoming radiation). In the Netherlands the amount of solar time in the summer is 4-5 hours whereas in the winter there this is only one hour. On average over the full year the Netherlands has 2.7 solar hours per day [14].

B.2 RF energy

RF energy harvesting is a specific type of wireless energy transfer, namely the far-field type. The other type, near field, is based on electric or magnetic induction, or magnetic resonance [43]. However, this type of energy harvesting requires a source to be within a few meters of the harvester. Since these are not present in the orchard nor practical to implement for a wireless sensor network, this type is disregarded.

An RF energy harvester utilises one or more antennas to collect ambient electromagnetic waves present in the air. The harvester also uses a rectifying circuit, which is needed because electromagnetic waves are time-varying field and therefore creates time-varying voltages at the antenna. In contrast, the load and energy storage unit require a DC input, so a rectifying operation is required. The electromagnetic waves originate from both natural and human-made sources. One of the natural sources is cosmic radiation from outer space, which is always present. Examples of human-made RF sources are wireless television broadcasting towers, radio towers, WiFi networks and cellular networks. Ambient RF power density is, therefore, higher in urban regions.

In order to relate the received power at the harvester to the transmitted power at the transmitter, Friis' transmission equation is used. Friis' equation is given in Equation B.3.

$$P_r = P_t \cdot G_t \cdot G_r \cdot (\frac{\lambda}{4\pi R})^2 \tag{B.3}$$

In this equation P_t is the transmitted power, G_t is the gain of the transmitting antenna, and G_r is the gain of the receiving antenna. The last term is the free-space loss, which depends on the wavelength λ and distance R. The energy that can be harvested depends on the efficiency of the antenna with the rectifying circuit and is equal to:

$$P_h = \eta \cdot P_r \tag{B.4}$$

Where η is the total efficiency of the antenna and rectifying circuit. The energy received can only be controlled by properly designing the receiving antenna gain, the efficiency of the antenna and the rectifying circuit. Since all other parameters are determined by the transmitting source they cannot be controlled.

The choice of the frequency band that is used to harvest RF energy is very important. This outcome differs per location and depends on which frequency bands are used for the transmission of electromagnetic waves, as well as distances to the transmission sources [44] [45]. Previous work has shown that it is possible to use RF energy as the only energy source to supply power to remote loads. Vyas [46] and Parks [21] have shown that a sensor node is powered from a digital TV signal in a frequency range of 500 MHz - 600 MHz, at a distance of 6.3 km and 10.4 km respectively.

B.3 Wind energy

The third type of ambient energy source that can be used to power the sensor nodes is wind energy. Wind energy is a type of kinetic energy that is indirectly related to solar energy. Due to uneven heating of the surface of the earth by the sun, a gradient of air temperature is created, and thereby also a gradient in air pressure. The air in high-pressure areas moves towards low-pressure areas, by which wind is created [47].

The kinetic energy of the wind can be harvested in several different ways, including harvesting with turbines, aeroelastic flutter generators and piezoelectric energy harvesters.

B.3.1 Wind turbine

In most wind energy harvesting applications, the kinetic energy from wind is harvested directly using a turbine. The wind turbine converts the kinetic energy of the wind into rotational energy of the blades and shaft by spinning the blades of the turbine. The turbine itself is connected to an electric generator, which converts the rotational energy of the turbine into electrical energy. The amount of power that can be generated using a turbine can be expressed by Equation B.5, in which A equals the area of the circle that is traced by the blades of the turbine in m^2, ρ the density of air in kg/m^3, v the velocity of the wind in m/s, and $C_p = \frac{P_{tur}}{P_{wind}}$ is the power coefficient. The power coefficient is the ratio of the power harvested to the total incoming wind power [48]. The theoretical limit of C_p is around $16/27 \approx 0.59$.

$$P_{tur} = C_p \frac{E}{t} = C_p \frac{\frac{1}{2}mv^2}{t} = C_p \frac{\frac{1}{2}(Avt\rho)v^2}{t} = \frac{1}{2} C_p A \rho v^3 \tag{B.5}$$

From this equation can be concluded that power that can be harvested is cubic related to the wind speed. Since the wind speed is generally not constant, the amount of harvested power varies with time. This means that with time there can be great fluctuations in the harvestable power. Because of the orientation of the wind, the placement of the turbine is very important, as the wind speed depends on several factors including weather, geographical location and local topographic circulations. Furthermore, there is a relation between the size of the turbine and the harvested power. This is the only factor that can be changed within the design, meaning that the turbine size can be altered to fit the power demands of the system.

B.3.2 Aeroelastic flutter generator

An alternative to a wind turbine is an aeroelastic flutter generator. This generator makes use of a strip of material that is put under tension and is connected to magnets surrounded by coils. When wind passes over this strip and the magnets start to vibrate, the motion of the magnets through the coils generates a current in the coils that can be captured and used in applications. Research has been conducted in this type of generator by Ramasur [49]. In his study is stated that this type of wind energy harvester generates more power than similarly sized small scale wind turbines, and operates in a wide range of wind speeds. Additionally, supplying a wireless sensor network with an aeroelastic flutter was successfully implemented for extended periods of time. Lastovicka-Medin [50] states that the aeroelastic flutter generator is a more cost effective alternative to a conventional wind turbine, and requires less maintenance due to the lack of rotating parts.

B.3.3 Piezoelectric energy

The piezoelectric effect is a process that converts kinetic energy in the form of vibrations into electrical energy. Piezoelectric materials have a crystalline structure that provides the unique ability to convert mechanical strain into electrical current. Often this current is much smaller than required for most electronic systems, but energy can be accumulated in capacitors or rechargeable batteries [19].

This energy harvesting solution could be implemented in this design by making use of the vibrations naturally occurring in the branches and trunks of trees due to wind. Sodano [19] argues that piezoelectric harvesting is most efficient if resonance occurs in the vibration, while random, ambient vibrations result in far smaller yield, which could potentially be a problem for this design. Furthermore, Sodano states that piezoelectric material is generally extremely brittle and is susceptible to accidental breakage, which could be hugely detrimental to the longevity and reliability of the system. In addition due to the high cost of the materials, the size of the piezoelectric generators is generally quite small, which results in a low efficiency. However, despite the lower efficiency, it is argued that the system still has advantages over wind turbines, such as lower maintenance due to the lack of rotating parts.

B.4 Thermal energy

The last type of ambient energy source for the sensor nodes is thermal energy. Thermal energy is obtained as a result of the specific heat capacity of material. The specific heat capacity is defined as the amount of

energy that must be provided to 1 kg of material in order to obtain a temperature increase of 1 kelvin. The specific heat formula is provided in Equation B.6, in which c is the specific heat capacity in $J \cdot kg^{-1} \cdot K^{-1}$, T is the temperature in kelvin and m is the mass of the material in kg.

$$Q = c * m * \Delta T \tag{B.6}$$

From the specific heat formula becomes clear that objects with a nonzero temperature contain thermal energy. In addition, the formula describes that in order to obtain a temperature difference, energy is either provided to or absorbed by the material. So by using a difference in temperature, energy can be harvested. The thermal energy harvesting is done by exploiting the Seeback effect. This effect describes the conversion of thermal energy into electrical energy. By using a thermoelectric generator (TEG) a temperature gradient can be converted into electrical power. Thermoelectric generators are usually used in situations were high-temperature components dissipate a lot of energy in terms of heat. Higher energy efficiencies can then obtained by recovering electrical energy from the heat.

B.4.1 The Seebeck effect

The direct conversion of thermal energy into electrical energy is denoted as the thermoelectric effect. The thermoelectric effect depends on the properties of the thermoelectric material: thermal conductivity, electric conductivity, Seebeck coefficient, and efficiency [13]. The thermoelectric effect itself is composed of four effects: Joule, Peltier, Thomson, and Seebeck effect, in which the last one is of most interest for the energy harvesting [13]. The Seebeck effect occurs in a circuit with two series-connected metallic conductors, in which there is a temperature difference between the two metal junctions. If one junction has a higher temperature T_{high} and the other junction has a lower temperature T_{low}, temperature gradient causes charge carriers to flow through the conductor junction. As a result, a Seebeck voltage is created for which the formula is provided in Equation B.7. In this Equation, α_a and α_b are the Seebeck coefficients of the material and α_{ab} is the thermopower in $V \cdot K^{-1}$.

$$V = \alpha_{ab} * (T_{high} - T_{low}) \tag{B.7}$$

For which:

$$\alpha_{ab} = \alpha_a - \alpha_b$$

The power of the thermoelectric generator is square dependent on the temperature difference between the junctions [13]. From this can be concluded that in order to obtain a TEG which generates a significant output voltage and output power, a large temperature difference is required.

Appendix C

RF energy analysis

C.1 Distance from GSM antennas

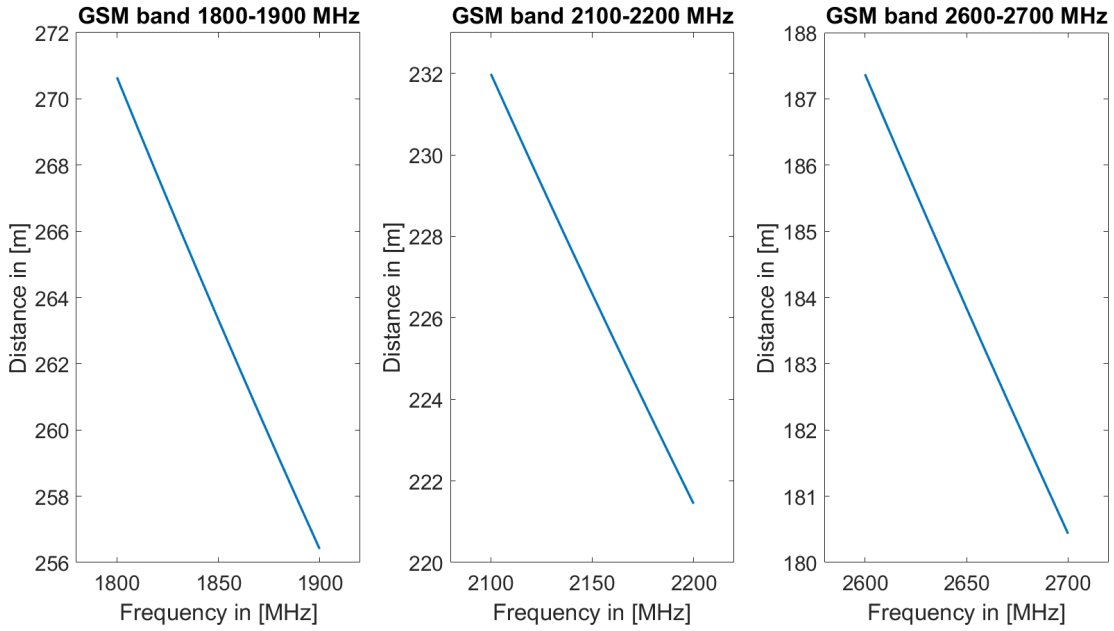

Figure C.1: In this figure the maximum distance the RF energy harvester proposed by Parks [21] can be located from a transmitting GSM antenna with frequencies available in the Netherlands [24], in order to harvest -15.43 dBm. In the left graph this is done for the GSM frequency range of 1800 - 1900 MHz, in the middle graph for 2100 - 2200 MHz and in the right graph for 2600 - 2700 MHz.

C.2 RF Energy test location

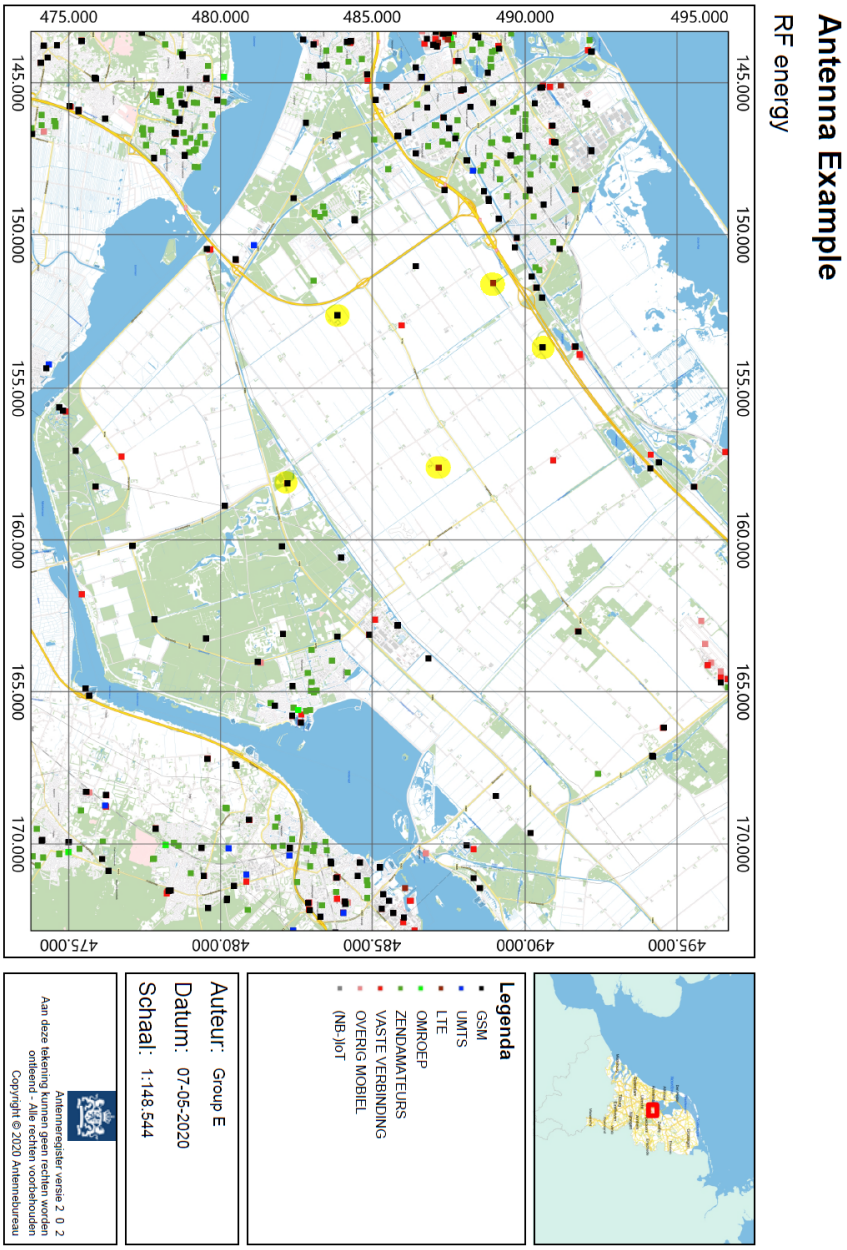

Figure C.2: This figure is obtained from the antenna-register of the Netherlands and shows the layout of the RF transmitting antennas in the GSM frequency range 800 - 950 MHz [22]. This layout is used as an example in Section 3.2.2.

The properties of the 5 highlighted antennas:

- Antenna 1
  - x = 2570 m
  - y = 3850 m
  - f = 940, 940, 955, 950 MHz
  - P = 35.5, 32.5, 34.8, 34.8 dBW
- Antenna 2
  - x = 1570 m
  - y = 9000 m
  - f = 800 MHz
  - P = 37.4 dBW
- Antenna 3
  - x = 3710 m
  - y = 10430 m
  - f = 940, 940, 816 MHz
  - P = 32.5, 35.5, 29.3 dBW
- Antenna 4
  - x = 7570 m
  - y = 7140 m
  - f = 800 MHz
  - P = 37.4 dBW
- Antenna 5
  - x = 8000 m
  - y = 2280 m
  - f = 942, 940, 930,930,806,816 MHz
  - P = 34.1, 28.1, 30.7, 30.7, 33.2, 35.2 dBW

Appendix D

Components specifications

D.1 Solar cell specifications

Table D.1 shows the datasheet specifications of the solar cells that are candidates for the implementation of the energy harvesting module.

Table D.1: List of suitable solar cells with their properties.

Specifications	SM500K12L	SM400K10L	SM470K12L	SM340K10L
Producer:	IXYS	IXYS	IXYS	IXYS
Open circuit voltage:	8.29 V	6.91 V	8.29 V	6.91 V
Short circuit current:	21 mA	16.4 mA	19.5 mA	14.0 mA
Solar cell efficiency:	25%	25%	25%	25%
Maximum peak power:	132.3 mW	85.7 mW	122.5 mW	73.5 mW
Typical MPP voltage:	6.70 V	5.58 V	6.70 V	5.58 V
Typical MPP current:	19.8 mA	15.4 mA	18.3 mA	13.2 mA
V_{oc} temp. coef.:	-20.9 mV/K	-17.4 mV/K	-20.9 mV/K	-17.4 mV/K
I_{sc} temp. coef.:	9.5 $\mu A/K$	7.4 $\mu A/K$	0.01 mA/K	0.01 mA/K
Dimensions (L x W):	32 x 24 mm	33 x 15 mm	35 x 22 mm	34 x 16 mm
Type:	Monocrystalline	Monocrystalline	Monocrystalline	Monocrystalline
Price:	€5.78	€4.22	-	€3.51

D.2 MPPT module specifications

Table D.2 shows the datasheet specifications of the maximum power point tracking modules that are candidates for the implementation of the energy harvesting module.

Table D.2: List of suitable MPPT modules with their properties.

Specifications	SPV1050	AEM10941	BQ25570
Producer:	STmicroelectronics	E-peas	Texas Instruments
Input voltage range:	75 mV - 18 V (V_c [1] 550 mV)	50 mV - 5.0V (V_c 380 mV)	100 mV - 5.1 V (V_c 600 mV)
Peak input power:	400 mW	550 mW	510 mW
Output voltage range:	LDO: 1.8 V & 3.3 V	LDO: 1.2/1.8 V & 1.8/4.1 V	2.0 V - 5.5 V
Output current:	200 mA	20 mA & 80 mA	110 mA
Storage voltage range:	2.2 V - 5.3 V	0 V - 4.5 V	2.0 V - 5.5 V
Charge current:	70 mA	-	185mA buck, 230 mA boost
Storage:	Supercapacitor o.a.	Supercapacitor o.a.	Supercapacitors o.a.
Control topology:	Buck-boost	Boost	Boost
Temperature op. range:	-40 °C up to 125 °C	-40 °C up to 125 °C	-40 °C up to 125 °C
Frequency:	1 MHz	-	1 MHz
Highest Efficiency:	92%	96%	93%
Cost:	€1.357	€4.00	€3.19
MPPT:	Yes, programmable	Yes, programmable	Yes, programmable
Quiscent current:	2600 nA, 1 nA	600 nA	488 nA, 3 0nA
Shut off mode:	Automatic	Automatic	Automatic/controllable

BQ25504	LTC3105	LTC3129
Texas Instruments	Linear Technology	Linear Technology
130 mV - 3 V (V_c 600 mV)	0.225 V - 5 V (V_c 250 mV)	1.92 V - 15 V (V_c 2.25 V)
400 mW	-	-
2.5 V - 5.25 V	LDO: 1.4 V-5 V	N.A.
-	12 mA	N.A.
2.5 V - 5.25 V	1.6 V - 5.25 V	1.4 V - 15.75 V
-	500 mA	200 mA/
Supercapacitors o.a	Supercapacitor o.a.	Supercapacitor
Boost	Boost	Buck-boost
-40 °C up to 125 °C	-40 °C up to 85 °C	-40 °C up to 125 °C
1 MHz	-	1.2 MHz
92%	91 %	95 %
€1.91	€3.04	€2.72
Yes, programmable	Yes, programmable	Yes, programmable
330 nA, -	24 μA, 10 μA	1.3 μA, 10 nA
Automatic	Automatic/controllable	N.A.

[1] The cold start voltage V_c is the minimal voltage required at the input of the module to start harvesting energy.

D.3 Storage module specifications

Table D.3 shows the datasheet specifications of the supercapacitors that are candidates for the implementation of the energy storage module.

Table D.3: List of suitable energy storage modules with their properties.

Specifications	SCMT32F755SRBA0	SCMU33F156SRBA0	SCMT22F505PRBA0	MAL219691204E3
Producer	AVX Corporation	AVX Corporation	AVX Corporation	Vishay
Capacitance	7.5 F	15 F	5 F	15 F
Rated voltage	5.5 V	5.5 V	5.5 V	5.6 V
Peak current	10.86 A	23.57 A	7.86 A	70 mA
Leakage current	78 μA	85 μA	30 μA	120 μA
DC ESR	120 $m\Omega$	50 $m\Omega$	150 $m\Omega$	10 Ω
Price	€3.12 (from 500)	€4.51 (from 9000)	€2.49 (from 5000)	€5.54 (from 1000)
Life cycles	500 000 cycles	500 000 cycles	500 000 cycles	50 000 cycles
Capacitor tolerance	-10%+30%	-10%+30%	-0%+100%	-20% +80%

MAL219690102E3	DGH505Q5R5
Vishay	Cornell Dubilier - CDE
90 F	5 F
5.6 V	5.5 V
3 A	8.4 A
500 μA	30 μA
180 $m\Omega$	120 $m\Omega$
€11.83 (from 500)	€1.95 (from 5000)
50 000 cycles	500 000 cycles
-20% +80%	-10%+30%

Appendix E

Matlab, PSpice Simulations

E.1 Solar cell simulation

As explained in Section 4.1.2 the solar cell that is used for the implementation of the energy harvesting module is the SM500K12L from IXYS. To make sure the implementation of the energy harvesting control modulate is done correctly, the solar cell is simulated using the program Simulink in Matlab. The simulation in Simulink uses a standard model of a solar cell based on a more elaborate version of the characteristic equation of a PV cell. The formula of the model is provided in Equation E.1 and can be seen as an extension on Equation B.2.

$$I = I_{ph} - I_s(e^{\frac{V+IR_s}{NV_t}} - 1) - I_{s2}(e^{\frac{V+IR_s}{N_2V_t}} - 1) - \frac{V+IR_s}{R_p} \tag{E.1}$$

The model provided in Equation E.1 can be seen as a circuit implementation, of a current sources I_ph connected to a parallel connection of two diodes $D1$ and $D2$ and resistor R_p. There is also a connection to the output terminals of the solar cell via a series resistance R_s. The circuit implementation of the solar cell is provided in Figure E.1.

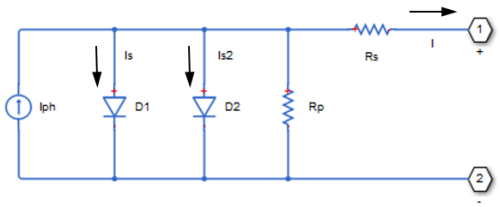

Figure E.1: Model circuit of the solar cell as implemented in Simulink.

This model of the solar cell is implemented in a test circuit provided in Figure E.2

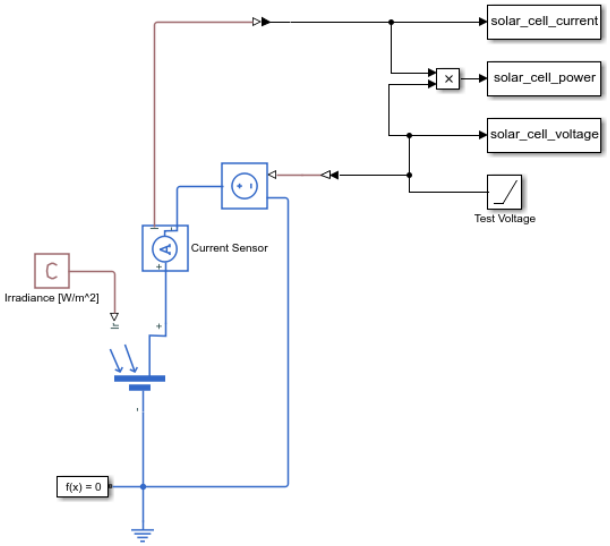

Figure E.2: Simulation circuit layout of solar cell in Simulink.

Figure E.2 show that the solar cell is exposed to a constant solar irradiation. The simulations are done at a temperature of 25 °C, for illumination intensities of 200, 400, 600, 8000, 1000 W/m^2. The parameters for modelling the solar cell are determined using the datasheet and Table D.1 and are set as follows:

- Short circuit current = 21.0 mA
- Open circuit voltage 8.29 V
- Irradiance used for measurements = 1000 W/m^2
- Quality factor = 1.4
- Series resistance = 0.151 Ω
- Amount of internal series connected cells = 12
- Maximum peak power = 0.1323 W
- First order temperature coefficient for Iph = 9.5e-6 $1/K$
- Energy gap = 1.12 eV

The result of the simulation that uses these parameters as an input, is provided in Figure E.3. This figure shows, on the left, the voltage-current characteristics of the solar cell when it is exposed to sunlight. The right figure shows the converted power when the solar cell is operated at a particular operation voltage. It can be concluded that the delivered power of the solar cells is maximised if it is operated at a terminal voltage between 6.4 V and 7.0 V depending on the irradiance. This is at all times around 84% of the open-circuit voltage.

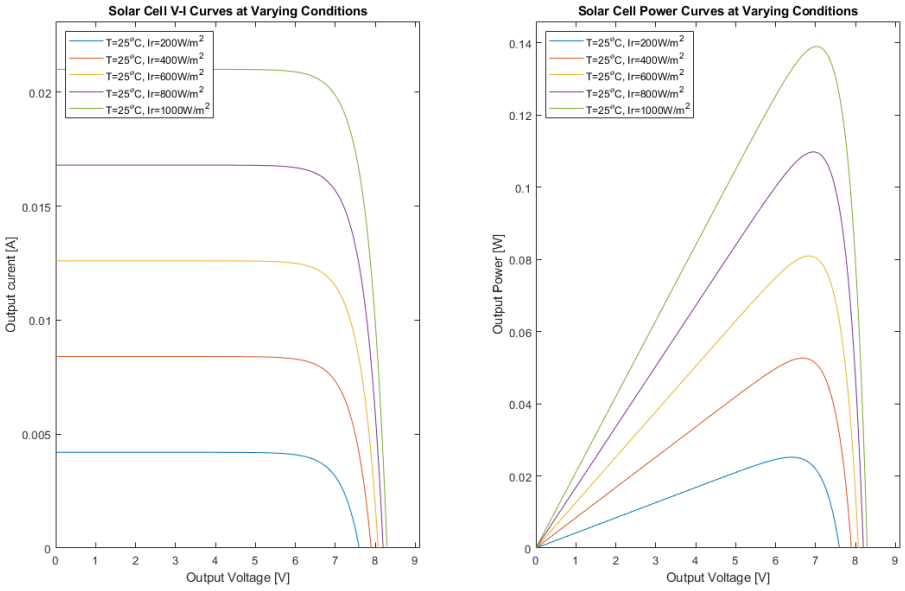

Figure E.3: Result of solar cell simulations in Simulink.

E.2 Single diode implementation simulation

The simulation model used to simulate the efficiency of charging the supercapacitor using the solar panel and a diode as control module, as explained in Section 4.2.1, is shown in Figure E.4. The current produced by the solar cell, the voltage over the solar cell, and the voltage over the supercapacitor are measured, depending on the irradiance on the solar cell. The output power of the solar cell is measured by multiplying the voltage and current of the solar cell. All these values are send to the workspace of Matlab. The model of the solar cell as mentioned in Appendix E.1 is used, and the model of the supercapacitor is a series connection of an ideal 5 F capacitor with a 120 $m\Omega$ resistor.

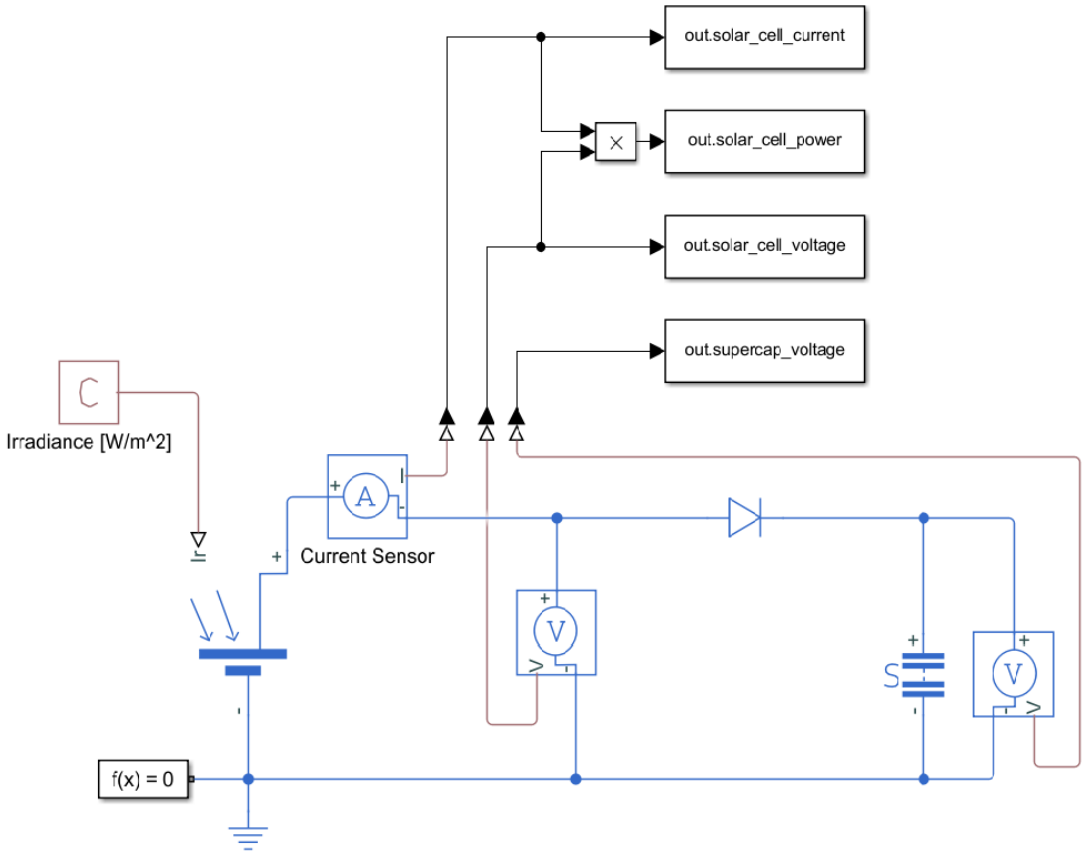

Figure E.4: Simulation model used for the simple diode implementation.

E.2.1 Diode simulation

The diode used is the Vishay RB751, as explained in Section 4.2.1. An exponential model of the diode is used, given by equation E.2, since this gives the most accurate simulation. Here I_s is the saturation current, q is the elementary charge of an electron, k is the Boltzmann constant, V is the voltage over the diode, and T the temperature in Kelvin.

$$I = I_s \cdot (e^{\frac{qV}{nkT}} - 1) \tag{E.2}$$

Simulink supports multiple parameterisation options to simulate the diode, where each option requires different characteristics of the diode. The parameterisation used is two current-voltage data points, obtained from the datasheet of the RB751 diode [33]. No charge dynamics are included, and no temperature dependence is included. The data used is the following

- Currents [I1 I2]: [0.1, 1.0] mA
- Voltages [V1 V2]: [240, 370] mV
- Ohmic resistance, RS: 25 Ohm
- Measurement temperature: 25 $degC$
- Number of series diodes: 1
- Number of parallel diodes: 1
- Reverse breakdown voltage: 40 V
- Junction capacitance: 2 pF

E.3 Energy monitoring implementation simulation

The energy level voltage monitoring system is simulated in Orcad-PSpice. In Figure E.5 the PSpice schematic is shown, together with the different probes used to measure voltages and currents. The simulation uses the component libraries of the Nexperia BSH105, Todhiba 1SS307E and Texas Instruments TLV8801. These libraries help to create an application-specific and accurate simulation of the circuit. In the figure voltage source $V1$ represents the supercapacitor, and voltage source $V3$ represents the output of the MCU, which is asserted when a measurement is required.

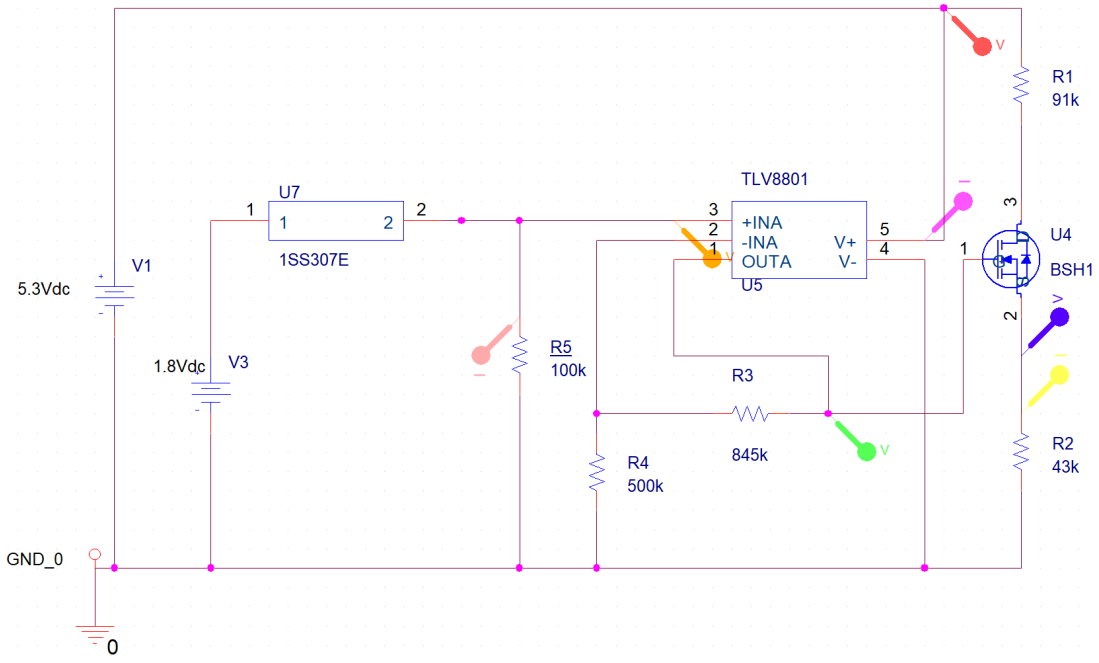

Figure E.5: Schematic of the simulated circuit of the energy monitoring circuit.

The simulation is done for three different cases of $V_{MCU\_on/off}$. At first, one where the MCU requires a measurement by asserting the input terminal, so $V3$ is set to 1.80 V. The second simulation is done when the MCU does not require a measurement, and the input terminal is deasserted, so $V3$ is set to 0.0 V. Finally one where the MCU does not require a measurement but due to the non-ideal terminal of the MCU, $V3$ is set to 0.45 V. All simulations are done by varying the supercapacitor voltage between 2.2 V and 5.4 V. Simulating for lower voltages is not needed, because then the SPV1050 does not the LDOs to operate, so no measurements can be done.

Figure E.6 shows the result of the simulation for the case when the energy monitoring circuit is in use. In Section 5.3.2 the intended relation between the supercapacitor voltage and the output V_{MCU_level} is already verified. Figure E.6 additionally shows the applied gate voltage, the current flowing into the op-amp, the current drawn from the MCU and the current flowing through drain of the MOSFET. The gate voltage follows the supercapacitor voltage until it reaches 3.2V and remains at this voltage for higher supercapacitor voltages. The opamp current also saturates at this voltage with a value of 2.88 μA, which is 0.50 μA more than the expected current through the feedback network. This is due to the internal power losses of the op-amp. Therefore, the op-amp operates as designed. Also, the current through the voltage divider, indicated as I_{drain}, is 39.55 μA at 5.3 V, and has a linear relation with the supercapacitor voltage. Finally, the current delivered at MCU_on/off is 11.88 μA which coincides with the estimate current in Section 5.3.1.

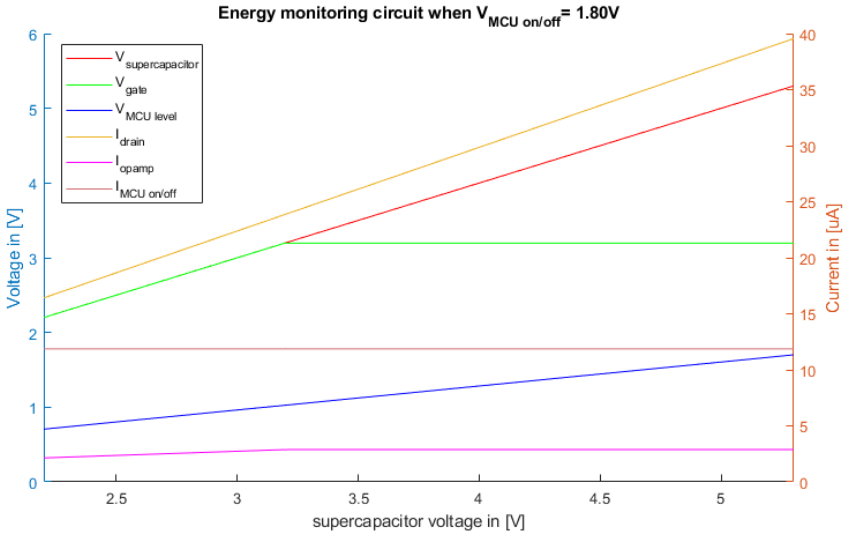

Figure E.6: Plot of the simulated characteristics of the energy monitoring circuit. The graph shows the currents and voltages of the energy monitoring circuit as a function of the supercapacitor voltage when the MCU_on/off is set high, 1.80 V.

In addition to the simulation for the case when the energy monitoring circuit is in use, the circuit is also simulated in shut off mode. Figure E.7 shows the result of this simulation in the form of the circuit voltages and currents that are obtained if $V_{MCU\_on/off}$ is set at 0.0 V. The figure clearly shows that if the supercapacitor voltage is increased the voltages at the gate of the transistor and input of the MCU stay close to zero. This satisfies the expectations of the design as discussed in Section 5.3.1. Also, the quiescent currents are more or less constant at 0.51 μA flowing through the opamp and 0.71 μA flowing through the MOSFET. The opamp current satisfies the design expectations, whereas the MOSFET current is a factor 7.1 higher than was specified in the datasheet [37]. This can be explained since the gate voltage of the transistor is not perfectly zero due to the output bias of the opamp. The nonzero gate voltage causes a higher current to flow which is an acceptable compromise. With these observations it can be concluded that the design operates as intended.

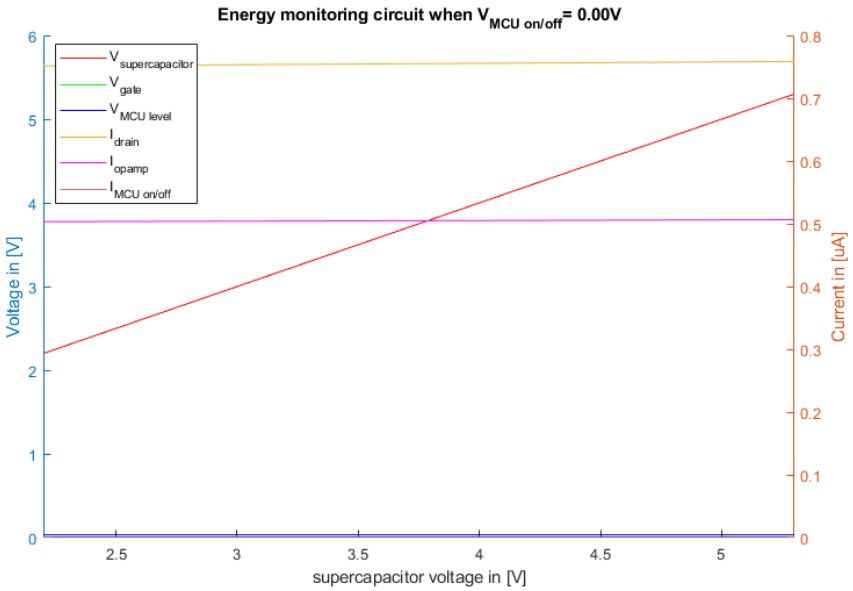

Figure E.7: Plot of the simulated characteristics of the energy monitoring circuit. The graph shows the currents and voltages of the energy monitoring circuit as a function of the supercapacitor voltage when the MCU_in is set low, 0.00 V.

Comparing Figure E.8 to Figure E.7, it can be concluded that the effect of the non-ideal MCU_on/off pin is minimal. When $V_{MCU\_on/off}$ is set at 0.45 V, the energy monitoring circuit performs similar to when it is fully shut off. The figure clearly shows that if the supercapacitor voltage is increased the voltages at the gate of the transistor and input of the MCU stay close to zero. The only significant change with respect to figure E.7 is the current delivered at MCU_on/off which is 0.07 μA rather than zero. The energy level monitoring circuit has therefore been correctly designed to counteract the noise generated by the MCU output pin.

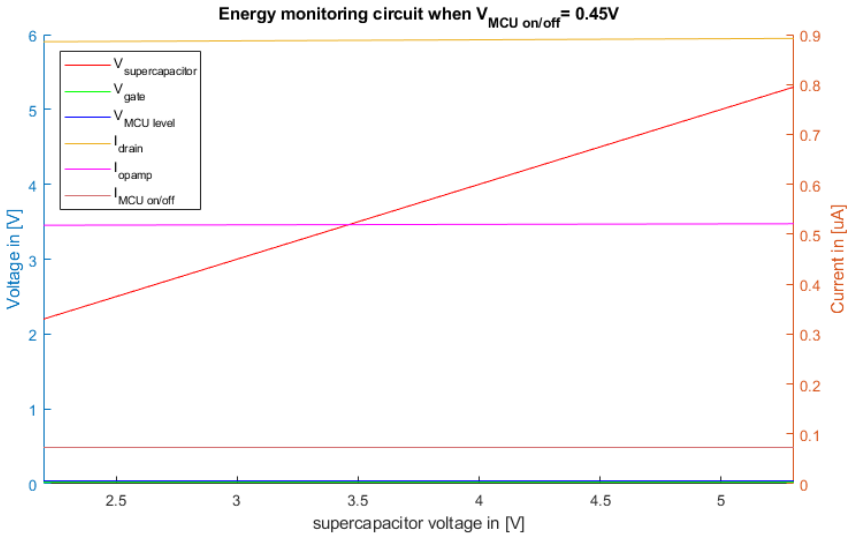

Figure E.8: Plot of the simulated characteristics of the energy monitoring circuit. The graph shows the currents and voltages of the energy monitoring circuit as a function of the supercapacitor voltage when the MCU_on/off is set at a worst case low of 0.45 V.

E.4 SPV1050 simulation

In Chapter 6 the design implementation of the SPV1050 as the main control module of the energy harvesting unit is discussed. In that chapter, the component values of the implementation were chosen such that the control module fits the implementation with the SM500K12L solar cell, DGH505Q5R5 supercapacitor and the energy level monitoring circuit. In order to verify whether the SPV1050 design implementation meets the specification, a simulation is done in Orcad-PSpice. This simulation is created using the SPV1050 component library provided by STmicroelectronics [32].

E.4.1 Simulation set up

Figure E.9 shows the circuit of the SPV1050 as it is implemented for the simulation. The figure indicates the solar cell and supercapacitor implementation in the orange rectangles. In this simulation, it is chosen to connect no loads to the LDO outputs of the SPV1050 module in order to prevent the load from interfering with the output voltage. In Figures E.10 and E.11 the results of the simulation are shown for the case where supercapacitor is initially charged to 4.0 V and 0.0 V respectively. It should be noted that the simulations showed took around 8 hours to run, and therefore only a time less than 300 ms is simulated. The probe signals that are measured during the simulation are defined as follows:

- IN_HV: The input voltage of the SPV1050 module, which is equal to the voltage over the terminals of the solar cell.
- $BATT$: The voltage across the supercapacitor.
- $STORE$: The voltage of the store capacitor, denoted as $C7$ in Figure E.9 or $C3$ in Figure 6.1.
- $LDO1$: The output voltage of the LDO that provides 1.8 V.

- $LDO2$: The output voltage of the LDO that provides 3.3 V.
- MPP: The signal that is used as a high-reference for finding the MPP_{Ratio}.
- MPP_SET: The signal that is used as a setpoint-reference for finding the MPP_{Ratio}. This ratio is found by sampling V_{MPP}/V_{MPP_set}.
- UVP: The signal that defines the under-voltage protection, if the signal drops below 1.23 V the under-voltage protection is activated and the switch between the $BATT$ and $STORE$ is opened.
- EOC: The signal that defines the end-of-charge voltage to protect the supercapacitor from over-charging. When signal exceed 1.23 V the switch between the $BATT$ and $STORE$ is closed and $C7$ discharges over the supercapacitor.
- $BATT\_CHG$: The signal that is used to indicate if the supercapacitor is charging and is pulled down if this is the case.
- $BATT\_OK$: The signal that is used to indicate if the switch between the $BATT$ and $STORE$ pins is closed. If the switch is closed, this pin is pulled down.

E.4.2 Normal operation

Figure E.10 shows the results of the simulation of the SPV1050 implementation when the supercapacitor is initially charged to 4.0 V. Starting at 0 ms, the capacitor $C1$ is being charged directly by the solar cell. The switch between the $BATT$ and $STORE$ is initially open such that the 4 V of the supercapacitor is not found in the remaining circuit. In order to find the MPPT reference voltage, the open-circuit voltage of the solar cell is measured between 25 ms and 113 ms. This is done by internally disconnecting the IN_HV terminal. and at time 113 ms measuring the open-circuit voltage V_{OC}, maximum power point high-reference and setpoint-reference. According to the figure this resulted in V_{IN_HV}=8.29 V, V_{MPP} = 1.71 V and V_{MPP_set} = 1.37 V. The MPP_{Ratio} is therefore set at a factor 1.37/1.71= 0.801 of the open-circuit voltage, 0.81*8.29= 6.64 V. This is also showed in the simulation where after 117 ms the V_{IN_HV} is kept constant at 6.57 V. The MPPT implementation of the SPV1050 therefore completely satisfies the expectation. After the MPPT measurement, the SPV1050 starts its normal operation and the capacitor $C7$ is charged by the solar cell. At time 131 ms the voltage at the $STORE$ terminal hits the end of charge voltage and V_{EOC} is equal to 1.23 V. As a result, the switch between the $BATT$ and $STORE$ terminals is closed and $C7$ discharges over the supercapacitor. Because the supercapacitor voltage is higher than the UVP, the switch stays closed and the capacitor $C7$ charges together with the supercapacitor as indicated in the figure. Figure E.10 also makes clear that at time 131 ms the LDOs start operating as expected, $LDO1$ and $LDO2$ give 1.8 V and 3.3 V respectively.

E.4.3 Startup

In Figure E.11 the result of the simulation is shown where the supercapacitor is initially set at 0 V. After the input capacitor is charged, the open-circuit voltage V_{OC} at IN_HV is measured, which occurs between 25 ms and 113 ms. At 113 ms this value is sampled and has a value of 8.29 V. Also, the values of MPP and MPP_SET are sampled at this time, and are equal to 1.72 V and 1.37 V respectively. The MPP_{ratio} equals 1.37/1.72 = 0.797. The MPP tracking accuracy of the SPV1050 is 95%, thus the minimum allowable ratio is $0.95 \cdot 0.8 = 0.76$. Therefore, the MPP_{Ratio} is correct. Then, the MPP voltage is set at IN_HV by multiplying MPP_{ratio} with V_{OC}, which equals 6.60 V. After 113 ms, the voltage of IN_HV is measured to be 6.57 V, and is therefore correct. At 113 ms the first cycle starts. From 113 ms until 132 ms, the voltage of $STORE$ keeps increasing until it reaches its end of charge voltage V_{EOC}. This voltage is equal to 5.26 V. The datasheet shows that it has an accuracy of -1%, and with the designed 5.27 V this results in a lower limit $V_{EOC,min}$ of $0.99 \cdot 5.27 = 5.21V$. Therefore it can be concluded that V_{EOC} value is correct. The two LDO's are turned on at the moment the V_{EOC} value is reached. At 137 ms, the $BATT$ and $STORE$ pins are connected, which can be seen by the fact that the signal $BATT\_OK$ drops to 0 V, until the under-voltage protection V_{UVP} is reached, which happens almost immediately, and these pins are disconnected again, which can be seen by the fact that $BATT\_OK$ rises to 5 V again. The measured value of V_{UVP} equals 2.20 V, which is exactly the intended value. The voltage of $LDO2$ drops to the V_{UVP} voltage at this point. This is the end of the first cycle, and this cycle then keeps repeating. It is expected that this happens until the voltage of $BATT$ reaches V_{UVP}, whereafter Figure E.10 shows the behaviour of the module.

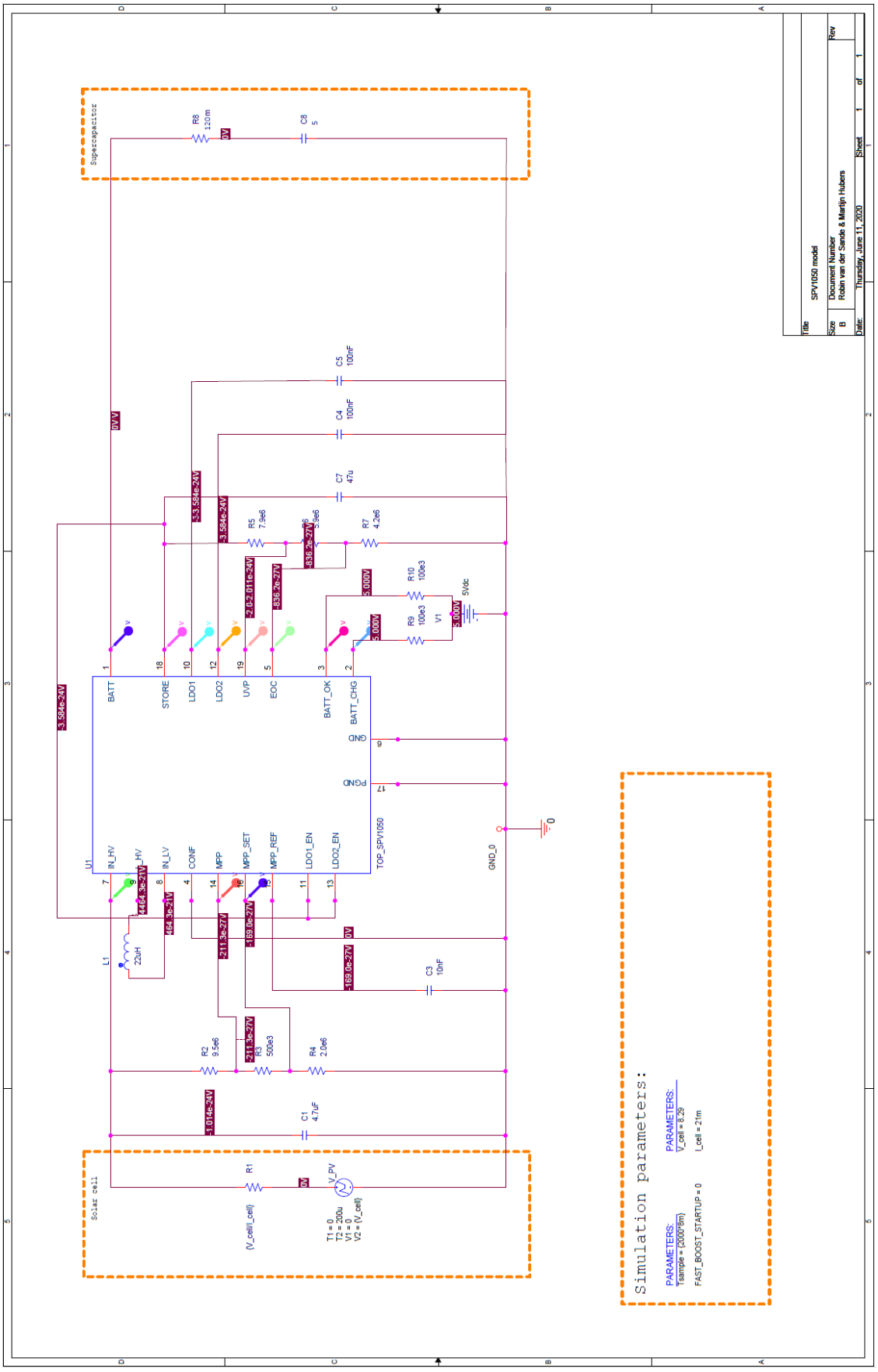

Figure E.9: Schematic of the simulated circuit of the SVP1050.

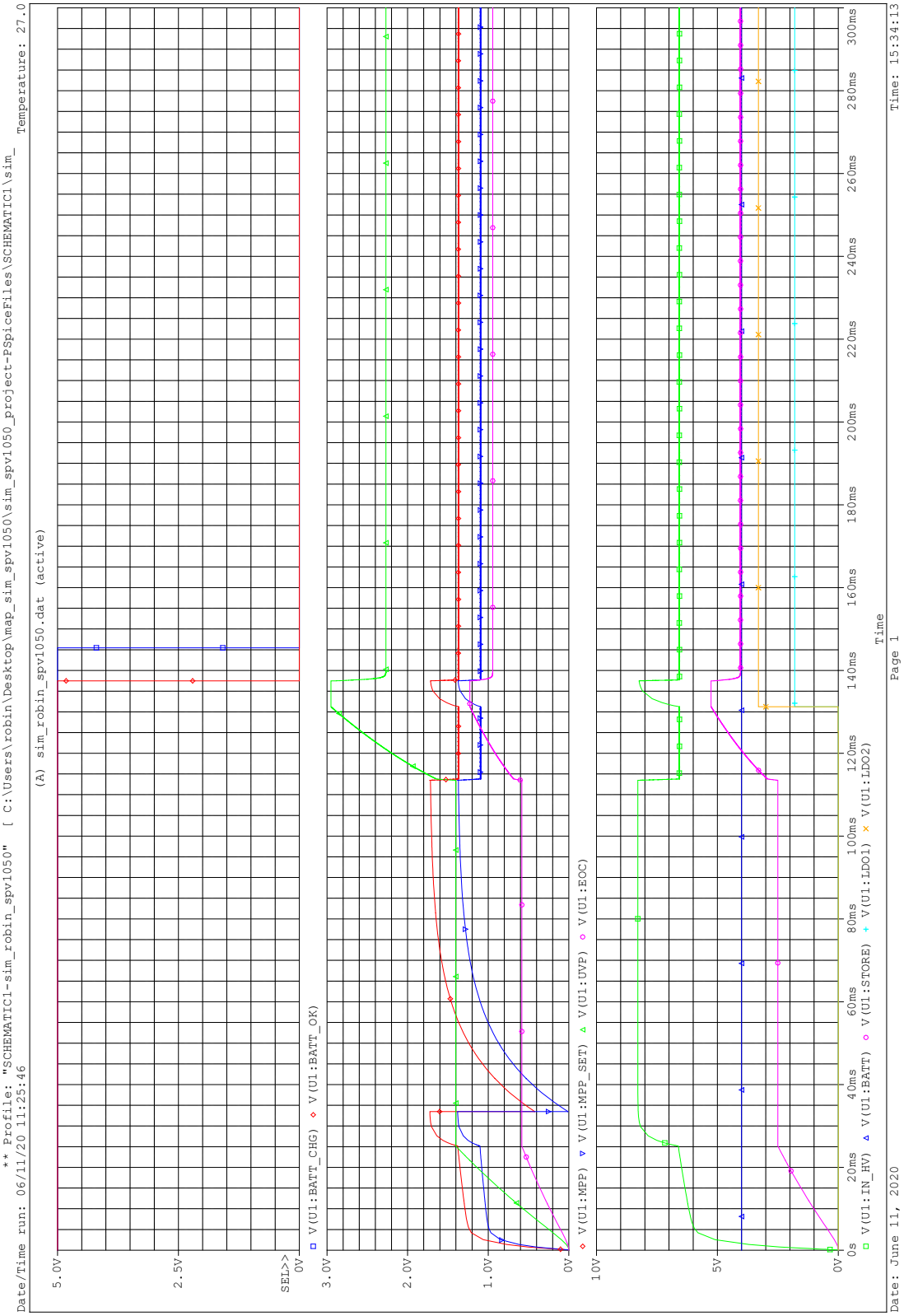

Figure E.10: PSpice simulation of the signals of the SPV1050 if the supercapacitor is set initially at 4.0 V.

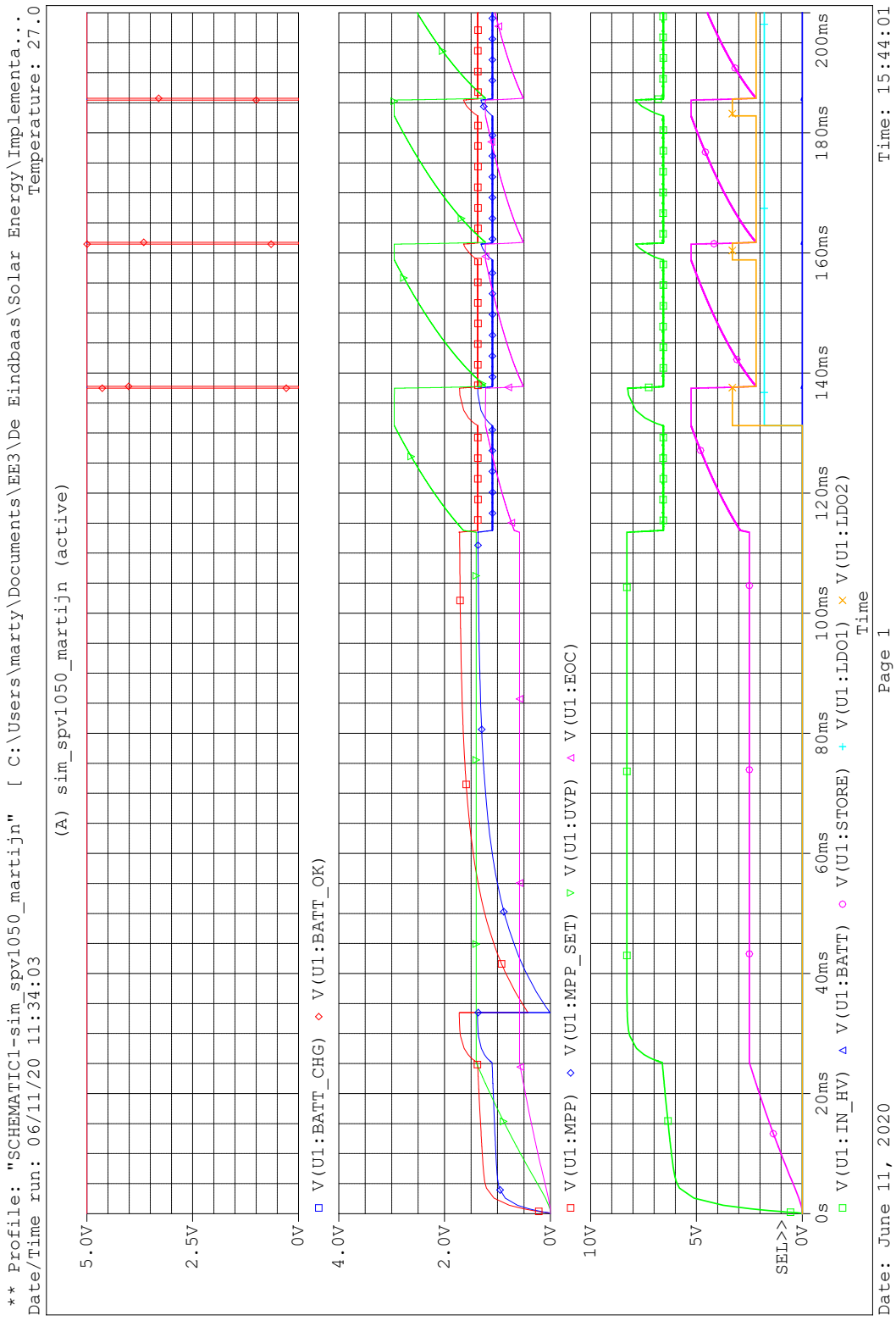

Figure E.11: PSpice simulation of the signals of the SPV1050 if the supercapacitor is set initially at 0.0 V.

E.5 System reliability analysis

In Section 6.2 the complete system reliability analysis was introduced. This simulation is used to verify the long term operation of the implemented energy harvesting and control module. The simulation is based on the top-level power breakdown, assumptions A1, A2 and A4-A6 and the weather data from February till June in the years 2009-2019.

The simulation in Section 6.2 is done for a supercapacitor that is initially charged for 80%. The same simulation is done with the initial condition that the supercapacitor is 0% charged. The result of this simulation is provided in Figure E.12. The simulation is based on the same temperature and solar irradiance data as provided in figure 6.2b.

From Figures 6.2b and E.12 can be concluded that the incident solar energy is high enough for the supercapacitor to be fully charged each day. As mentioned in Section 5.2, the solar cell is capable to fully charge the supercapacitor. So if the supercapacitor ends up being empty, it is charged within a time-span of a day.

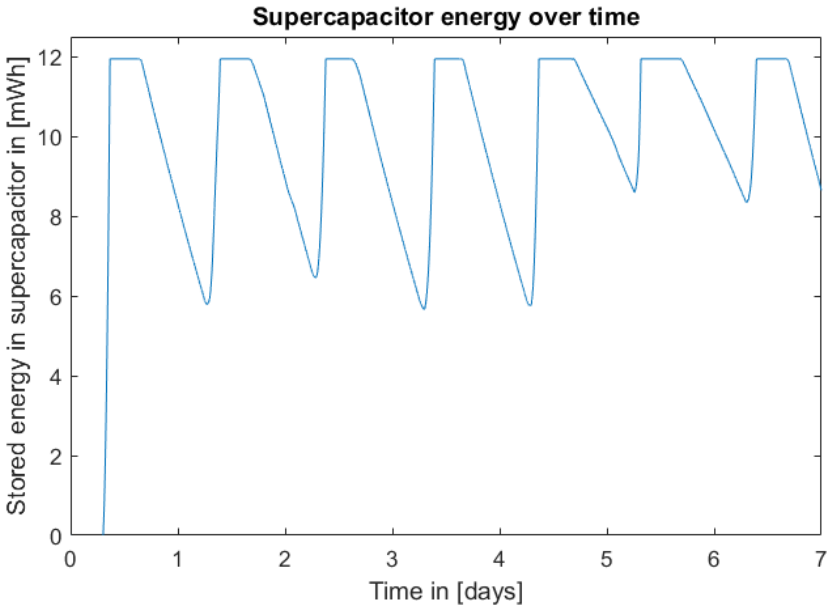

Figure E.12: This figure shows the energy level of the supercapacitor as a function of time if the designed energy harvesting and control module is used. The simulation is based on week 6 in 2009, and uses an initially 0% charged supercapacitor.

Another result of the complete system reliability analysis is provided in Figure E.13. This figure shows the energy level in the supercapacitor as a function of time for the period of February 2009 till June 2009. From this figure can be concluded that the energy level during spring stays well above the 0 mWh, so at all times enough energy is stored to perform the intended operations.

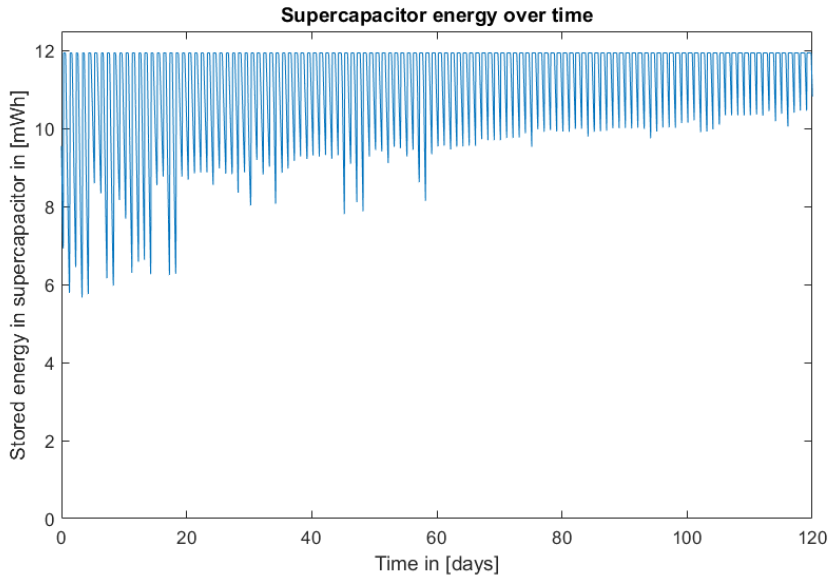

Figure E.13: This figure shows the energy level of the supercapacitor as a function of time using the designed energy harvesting and control module. The simulation is based on the time-period of February 2009 till June 2009, and uses an initially 80% charged supercapacitor.

In Section 6.2, the minimal energy level of the supercapacitor that was reached during a day is analysed. The lowest minimal energy of the supercapacitor that occurred in these 10 years of spring data is 5.45 mWh. This occurred in day 970 in the simulation. Figure E.14 gives the energy level in the supercapacitor as a function of time for that day. The solar irradiance and temperature during this period are provided in Figure E.15. From the figures can be concluded that this low energy level occurs as a result of a period of low ambient solar power, below 75 W/m^2, while also being subjected to temperatures far below the critical temperature. Notice that even under this worst-case scenario, the system performs as intended.

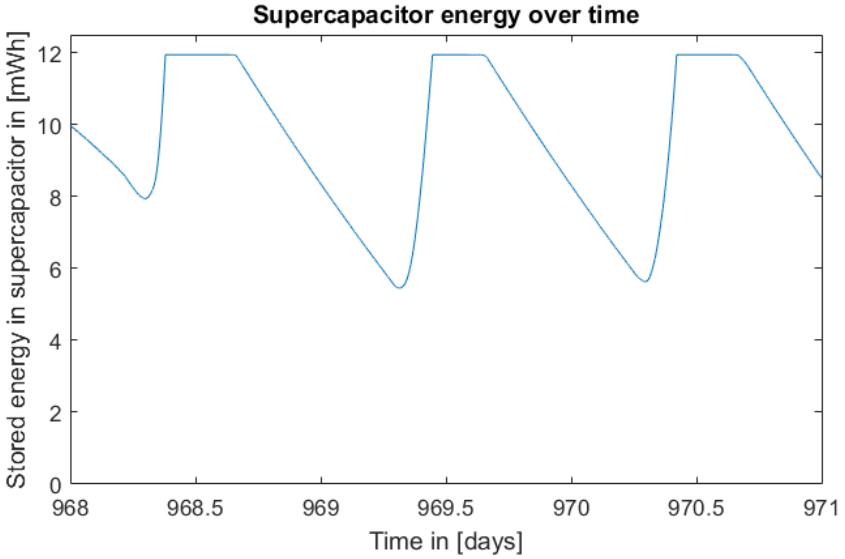

Figure E.14: This figure shows the energy level of the supercapacitor as a function of time using for the worst-case days.

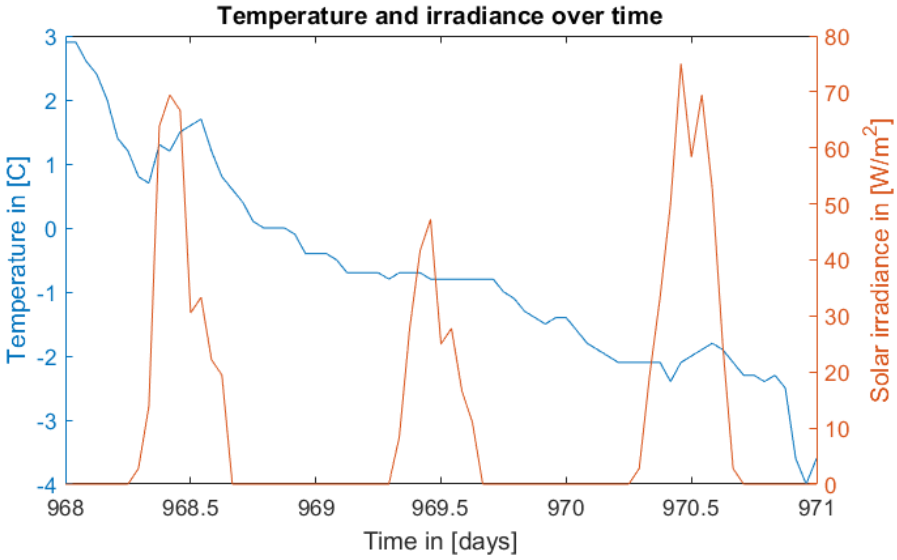

Figure E.15: This figure shows the temperature and solar irradiance for the worst-case days as used for Figure E.14